

A study of interacting galaxies from the Arp-Madore Catalogue: Triggering of star formation and nuclear activity

Pedro H. Cezar^{1,2}, Miriani G. Pastoriza³, Rogério Riffel^{1,3}, Cristina Ramos Almeida^{1,2}, Angela C. Krabbe⁴, and Sandro B. Rembold⁵

¹ Instituto de Astrofísica de Canarias, Calle Vía Láctea, s/n, 38205 La Laguna, Tenerife, Spain
e-mail: pedrocezar.astro@gmail.com

² Departamento de Astrofísica, Universidad de La Laguna, 38206 La Laguna, Tenerife, Spain

³ Departamento de Astronomia, Universidade Federal do Rio Grande do Sul, IF, CP 15051, Porto Alegre 91501-970, RS, Brazil
e-mail: riffel@ufrgs.br

⁴ Departamento de Astronomia, Instituto de Astronomia, Geofísica e Ciências Atmosféricas da USP, Cidade Universitária, 05508-900 São Paulo, SP, Brazil

⁵ Departamento de Física, CCNE, Universidade Federal de Santa Maria, 97105-900 Santa Maria, RS, Brazil

May 31, 2024

ABSTRACT

We present Gemini Multi-Object Spectrograph (GMOS) spectroscopic observations of 95 galaxies from the Arp & Madore (1987) catalogue of peculiar galaxies. These galaxies have been selected because they appear to be in pairs and small groups. These observations have allowed us to confirm that 60 galaxies are indeed interacting systems. For the confirmed interacting sample, we have built a matched control sample of isolated galaxies. We present an analysis of the stellar populations and nuclear activity in the interacting galaxies and compare them with the isolated galaxies. We find a median light (mass) fraction of 55% (10%) in the interacting galaxies coming from stellar populations younger than 2 Gyr and 28% (3%) in the case of the isolated galaxies. More than half of the interacting galaxies are dominated by this young stellar population, while the isolated ones have most of their light coming from older stellar populations. We used a combination of diagnostic diagrams (BPTs and WHAN) to classify the main ionization mechanisms of the gas. The interacting galaxies in our sample consistently show a higher fraction of active galactic nuclei (AGN) relative to the control sample, which ranges between 1.6 and 4 depending on the combination of diagnostic diagrams employed to classify the galaxies and the number of galaxies considered. Our study provides further observational evidence that interactions drive star formation and nuclear activity in galaxies and can have a significant impact on galaxy evolution.

Key words. galaxies: evolution – galaxies: interactions – galaxies: peculiar – galaxies: nuclei – galaxies: star formation – galaxies: active

1. Introduction

It is well known that galaxy interactions and merger events play an important role in the evolution of galaxies and, in particular, their star formation histories. Interactions have been suggested as the drivers of violent star formation events, producing some of the most luminous objects in the Universe (Sanders & Mirabel 1996). From early studies to the most recent ones, it has been found that star formation is enhanced in interactions and mergers as compared to isolated galaxies (Donzelli & Pastoriza 1997; Woods & Geller 2007; Knapen et al. 2015; Zaragoza-Cardiel et al. 2018; Pan et al. 2019; Azevedo et al. 2023). However, just a few studies focused on analysing the stellar populations of these galaxies, most of them dedicated to single or a few pairs (Krabbe et al. 2008, 2011, 2017; Alonso-Herrero et al. 2012; Dametto et al. 2014; Bessiere et al. 2014, 2017; Argudo-Fernández et al. 2015; Cortijo-Ferrero et al. 2017b,a; Rosa et al. 2018). As pointed out by Krabbe et al. (2017), this analysis is crucial to understand not only the star-forming regions photoionizing the gas but also the full history of stellar populations born in the interacting galaxies.

Galaxy interactions and mergers are also frequently associated with the triggering and feeding of Active Galactic Nu-

clei (AGN; see Heckman & Best 2014; Storchi-Bergmann & Schnorr-Müller 2019, and references therein for a wide list of publications in the theme). This relation, however, is not exempt from controversy. Several simulations show that galaxy interactions trigger AGN activity (Neistein & Netzer 2014; Gatti et al. 2015). In particular, Neistein & Netzer (2014) propose in their work that minor mergers could be the main triggers of low to intermediate-luminosity AGN. However, recent theoretical work shows that only 15% of the supermassive black hole (SMBH) growth is produced via galaxy mergers (Steinborn et al. 2018; McAlpine et al. 2020).

Observationally, several works found that in both radio-quiet and radio-loud AGN are more frequently hosted in galaxies showing signatures of morphological disturbance than non-active galaxies (Ramos Almeida et al. 2011, 2012; Ellison et al. 2019; Hernández-Toledo et al. 2023; Rembold et al. 2024), especially in the case of luminous quasars (Bessiere et al. 2012; Pierce et al. 2022, 2023; Araujo et al. 2023). Another approach is to look for galaxies undergoing an interaction to verify the prevalence of AGN using optical excitation diagnostics or multi-wavelength datasets. Once more, numerous works appear to indicate that interactions are capable of inducing and/or enhancing the nuclear activity (Pastoriza et al. 1999; Koss et al. 2010; El-

lison et al. 2011; Silverman et al. 2011; Satyapal et al. 2014; Fu et al. 2018; Jin et al. 2021; Steffen et al. 2023). However, some works did not find a significant excess of AGN in interactions relative to field galaxies (Cisternas et al. 2011; Böhm et al. 2013; Villforth et al. 2014; Karouzos et al. 2014; Argudo-Fernández et al. 2016; Marian et al. 2019; Silva et al. 2021; Villforth 2023). These discrepancies could be due to selection effects, including the AGN identification method (Satyapal et al. 2014; Ellison et al. 2019), different methodologies, and datasets. Pierce et al. (2023) argue that in the absence of deep imaging, tidal features may be missed, and the fraction of morphological disturbance observed in AGN hosts could be underestimated. The methodology used to identify AGN galaxies can also have an impact on the observed merger-AGN connection. Focusing on more advanced mergers, recent works targeting post-mergers (Li et al. 2023) and galaxies presenting gas-stellar rotation misalignment (Raimundo et al. 2023) show an excess of AGN relative to undisturbed galaxies.

In this paper, we analyze the stellar populations and ionized gas excitation mechanisms of a sample of galaxy pairs or small group candidates from the Arp & Madore (1987) catalogue of peculiar galaxies. The sample of galaxy pairs includes interacting galaxies with smaller companions (Category 1, when one of the galaxies has less than half of the primary size), interacting galaxies with similar sizes (Category 2), groups (Categories 3 and 4), and disturbed galaxies with jets or tails (Categories 7 and 15). We first use the spectroscopic observations to confirm or discard the interacting nature of the pairs. The confirmed physical systems are then compared to a control sample of isolated galaxies built to match the interacting sample properties. In this way, we expect to be comparing similar galaxies but in different environments. With this comparison, we aim to address the impact of interactions and mergers on the stellar populations and nuclear activity of the galaxies.

This paper is organized as follows: in Sec. 2 we present the observations, data reduction, and measurements used in this work. In Sec. 3 we show the results of the modelling of the stellar populations in the interacting and isolated galaxy samples. Sec. 4 presents the ionized gas and stellar populations extinctions. In Sec. 5 we show the results of the main excitation mechanisms responsible for ionizing the gas in the interacting and isolated samples. Sec. 6 focus on comparing the star formation strength of star-forming galaxies in the interacting and control samples. In Sec. 7 we discuss the results and finally, Sec. 8 summarizes our findings. Throughout this paper, we adopt the Hubble constant as $H_0 = 75 \text{ km s}^{-1} \text{ Mpc}^{-1}$ (Spergel et al. 2007).

2. Sample selection, observations, and analysis

Our parent interacting galaxy sample was selected from the Arp & Madore (1987) catalogue and it is composed of 43 candidates to pairs, small groups, and mergers. Most of them were selected from Category 1 (37/43 candidates), where one of the galaxies has less than half the size of its companion(s). Most of the main galaxies in Category 1 are spirals. The remaining six candidates are: AM 0338-320 (Category 2, pairs of galaxies of comparable sizes), AM 0103-502 (Category 3, triple systems), AM 0302-611 (Category 4, quartet systems), AM 2037-550 (Category 7, galaxies with jets), AM 2037-550, and AM 2220-661 (Category 15, galaxies with tails, loops of material, or debris). In total, these 43 galaxy systems comprise 100 individual galaxies. Most of these galaxies are infrared bright, and therefore, we expect a high incidence of star-forming and/or active galaxies.

2.1. Observations and data reduction

We present spectroscopic observations of 95 of the 100 galaxies included in our parent sample of 43 candidates to physical pairs, small groups, and mergers. To the best of our knowledge, these are the first spectroscopic observations for most of the sources. The sample is listed in Table A.1 in Appendix A, and further details are given in Section 2.2.

The data were obtained using the Gemini South Multi-Object Spectrograph (GMOS-S) at the Gemini-South telescope, under the “poor weather queue” programme GS-2007A-Q-240, between October 2007 and January 2008. The instrument configuration was the 0.5'' slit with the R150 grating binned to 2×4 pixels (spectral x spatial). Two grating settings were used, centred at 8700 and 8800 Å, in order to cover the chip gaps. This setup provided full spectral coverage from 3500 Å to beyond 8000 Å (rest wavelength), at a spectral resolution of 11 Å at 6356 Å - just enough to separate the [NII]+H α blend while at the same time covering the whole optical spectrum for redshifts up to ~ 0.2 . The slit was aligned to include the two galaxies in the pairs, and additional slit positions were used in the case of groups (see Fig. 1). The objects were nodded along the slit to improve sky subtraction. Exposure time was 1 h on source (2×900 s per grating setting).

The data reduction followed standard procedures, using the GEMINI.GMOS routine of the IRAF package (Tody 1986, 1993), except that no flat field correction was applied to the spectroscopic data presented here. This was due to the strong fringing effects present redwards of 750 nm, which severely degraded the quality of the data towards the red. For the large apertures extracted here, this has no measurable effect on the data. To make a fair comparison among the galaxies, we have extracted all the spectra in a consistent aperture of $2.2 \text{ kpc} \times 0.5''$ ($0.5'' \approx 380 \text{ pc}$ at the mean distance of the sample).

The imaging data shown in Fig. 1 correspond to the acquisition images taken just before the spectroscopy to centre the objects in the slit. The Sloan r' filter was used, and reduction was standard, including bias and flat-field corrections.

2.2. The interacting and isolated galaxies samples

The redshift for the interacting galaxies was measured using the IRAF tasks RVIDLINES and XCOR, for emission and absorption line spectra, respectively, and adopting $H_0 = 75 \text{ km s}^{-1} \text{ Mpc}^{-1}$ (Spergel et al. 2007). As in previous works, in order to determine if the galaxies belong to a physical system, we constrain the difference between their radial velocities to be $\Delta v_r < 500 \text{ km s}^{-1}$ (Patton et al. 2000; Lin et al. 2008; Ventou et al. 2017). Sixty galaxies were found to be in truly interacting systems (19 pairs and 6 small groups), although we only have GMOS-S spectra for 59 of them. We do not have a GMOS-S spectrum of AM 2106-624 G1 because the slit was misplaced, but it was confirmed as a member of the pair with AM 2106-624 G2 thanks to a previous radial velocity estimate (see Table A.2 in Appendix A). Therefore, the following analysis was carried out using the 59 interacting galaxies with spectra, which we will refer to as the interacting (INT) sample hereafter. For them we measured redshifts in the interval $0.006 \leq z \leq 0.097$. Figs. 1 and 2 show examples of r' filter acquisition images and observed optical spectra of confirmed pairs and groups. The remaining 40 galaxies include 22 that are just close in projection, and 18 for which either the data did not allow us to constrain their redshifts or were not available. Table A.2 in Appendix A presents the radial velocities for the interacting systems and Table B.1 in Appendix B for the non-

interacting galaxies, together with information about the sources which could not be either confirmed or discarded as interacting.

In order to find an adequate control sample of non-interacting galaxies (i.e., isolated sources), comparable in mass and redshift with those of our sample, we first used the broadband magnitudes (JHK) from the Two Micron All Sky Survey (2MASS) extended source catalogue (Skrutskie et al. 2006) of the INT galaxies as a proxy for their stellar mass (Davies et al. 2015). We then searched for galaxies with optical spectra in the Sloan Digital Sky Survey (SDSS) III Data Release 9 (DR9, York et al. 2000; Eisenstein et al. 2011; Ahn et al. 2012) matched in redshift and 2MASS JHK magnitudes in the extended source catalogue to each of the INT galaxies. The candidates to control sample galaxies for each INT galaxy were then visually inspected using the SDSS images available, and kept only those having similar morphologies as the interacting galaxy they match with in infrared magnitude and redshift. In particular, we searched for galaxies with the same galaxy type as each of the INT galaxies (i.e., spirals, lenticulars, or ellipticals) and stellar structures (i.e., bars, rings, and/or spiral arms) and we discarded galaxies with clear signs of interaction and/or close companions of similar mass at distances < 100 kpc.

We note that we selected just one control sample galaxy for each pair member of the INT sample, which is the minimum required for comparison while still being possible to analyse the galaxies individually. Fourteen of the interacting galaxies have either too disrupted optical morphologies or do not have infrared magnitudes available in the 2MASS database, thus no control sample galaxies were selected for them. We did not discard the INT galaxies without controls from the analysis because we checked that the results were consistent including them or not.

Our final control sample of isolated galaxies (CTR sample hereafter) consists of 45 objects, which match the INT sample in redshift, 2MASS J absolute magnitude, and morphology. Figure 3 shows the redshift and absolute J magnitude distribution of the INT and CTR samples. The median, mean, and Kolmogorov-Smirnov (KS) test p-values confirm the similarity between them. Table A.2 in Appendix A lists the INT galaxies, radial velocities, and the SDSS DR9 information of the corresponding CTR sample galaxies. The optical spectra of the CTR sample are from SDSS, which uses a 3'' fiber and covers the spectral range 3800–9200 Å, with a spectral resolution (R) varying from R~1500 at 3800 Å to R~2500 at 9000 Å. This corresponds to FWHM=2.78 Å at 7000 Å (Alam et al. 2015; Abolfathi et al. 2018).

2.3. Stellar populations modeling

To perform a stellar population analysis of the galaxies by means of full-spectral fitting of their spectra, we employed the STARLIGHT code (Cid Fernandes et al. 2005; Cid Fernandes 2018). This code combines the spectra of a set of N_\star simple stellar population (SSP) template spectra denoted as $b_{j,\lambda}$. These templates are weighted in varying proportions to replicate the observed spectrum O_λ . The modeling process involves normalizing both the observed and modeled spectra, represented as M_λ , at a user-defined wavelength λ_0 . The vector, x_j , represents the fractional contribution of the j th SSP to the light at the normalization wavelength λ_0 . Additionally, STARLIGHT incorporates a Gaussian distribution $G(v_\star, \sigma_\star)$ to address velocity shifts (v_\star) and velocity dispersion (σ_\star). The model spectra can be expressed as:

$$M_\lambda = M_{\lambda_0} \left[\sum_{n=1}^{N_\star} x_j b_{j,\lambda} r_\lambda \right] \otimes G(v_\star, \sigma_\star), \quad (1)$$

where M_{λ_0} represents the flux of the synthetic spectrum at the wavelength λ_0 . To account for reddening, it incorporates the term $r_\lambda = 10^{-0.4(A_\lambda - A_{\lambda_0})}$. In the process of fitting, the code searches for the best-fit parameters by minimizing χ^2 , defined as:

$$\chi^2 = \sum_{\lambda_i}^{N_f} [(O_\lambda - M_\lambda) \omega_\lambda]^2, \quad (2)$$

where ω_λ are the weights of each pixel in the fitting. For more details see Cid Fernandes et al. (2005).

We employ a "base of elements" known as the *GM*, as detailed in Cid Fernandes et al. (2013, 2014). This base is constructed using the MILES (Vazdekis et al. 2010) and González Delgado et al. (2005) models and has been updated with the MILES V11 models (Vazdekis et al. 2016). Our selection includes 21 ages ($t = 0.001, 0.006, 0.010, 0.014, 0.020, 0.032, 0.056, 0.1, 0.2, 0.316, 0.398, 0.501, 0.631, 0.708, 0.794, 0.891, 1.0, 2.0, 5.01, 8.91, \text{ and } 12.6$ Gyr) and four metallicities ($Z = 0.19, 0.40, 1.00, \text{ and } 1.66 Z_\odot$). See Riffel et al. (2021, 2023) and references therein for more details on applications of this base.

The normalization flux at λ_0 was chosen to be the mean value between 5650 Å and 5750 Å. The reddening law used was that of Cardelli et al. (1989), and the synthesis was performed in the spectral range from 3510 Å to 6930 Å (rest frame). An example of stellar population fitting is shown in Fig. 4 for the galaxy AM 1933-422 B.

2.4. Emission lines fitting

The rest-frame emission-line spectra, free from stellar absorption contribution, have been used to fit the strongest emission lines in the optical region. To this purpose we use the `ifscube`¹ Python package (Ruschel-Dutra & Dall'Agnol De Oliveira 2020; Ruschel-Dutra et al. 2021). The fitted emission lines are [O II] $\lambda\lambda 3726, 3729$, H δ , H γ , [O III] $\lambda 4363$, H β , [O III] $\lambda\lambda 4959, 5007$, He I $\lambda 5876$, [O I] $\lambda 6300$, H α , [N II] $\lambda\lambda 6548, 6583$, and [S II] $\lambda\lambda 6716, 6731$. The emission-line profiles are fitted with Gaussians by adopting the following constraints: (i) the width and centroid velocities of emission lines from the same parent ion are constrained to the same value; (ii) the centroid velocity is allowed to vary from ± 350 km s $^{-1}$ relative to the velocity obtained from the redshift of each galaxy; (iii) if necessary a broad component was added in the case of the HI lines to account for the broad line region emission. In addition, we include a first-order polynomial to reproduce the local continuum. We also applied a cut in signal-to-noise, requiring that the emission line amplitudes must be larger than the noise level computed in the line region after the fit in order to have reliable emission line measurements. The emission line flux errors were estimated using the empirical relation described in (Lenz & Ayres 1992; Wesson 2016). An example of the emission line fitting is shown in Fig. 5.

The extinction correction was made using Balmer decrement, considering case B for recombination, with $N_e = 100$ cm $^{-3}$ and $T_e = 10\,000$ K, given an intrinsic ratio of H α /H $\beta = 2.86$ (Osterbrock & Ferland 2006) and the extinction law of Cardelli et al.

¹ <https://github.com/danielrd6/ifscube>

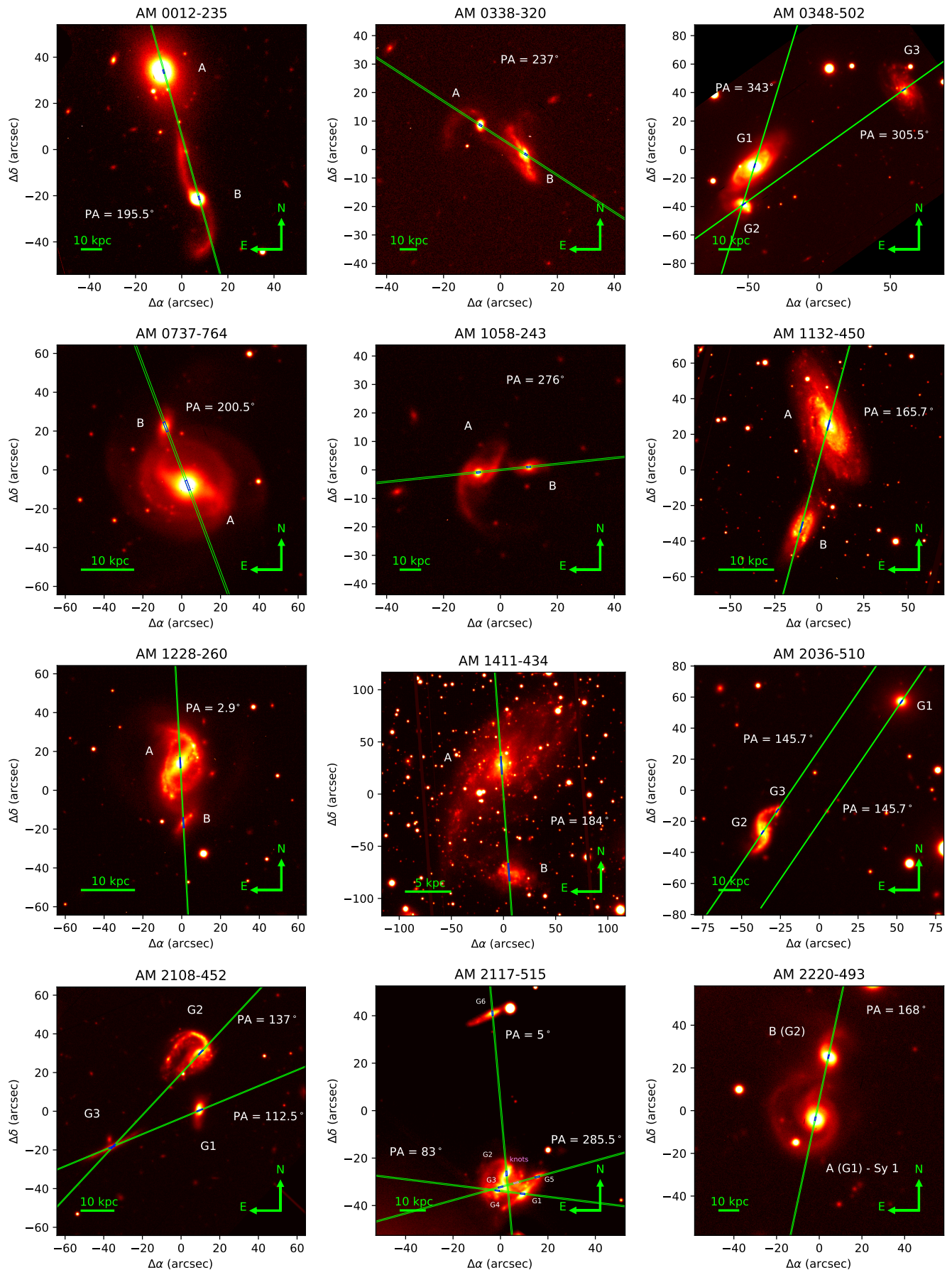


Fig. 1. Examples of r' filter acquisition images obtained with GMOS-S of the interacting pairs and groups. The slits are represented in green, with the nuclear aperture used here shown in blue. The remaining images are shown in Fig. A.1 in Appendix A.

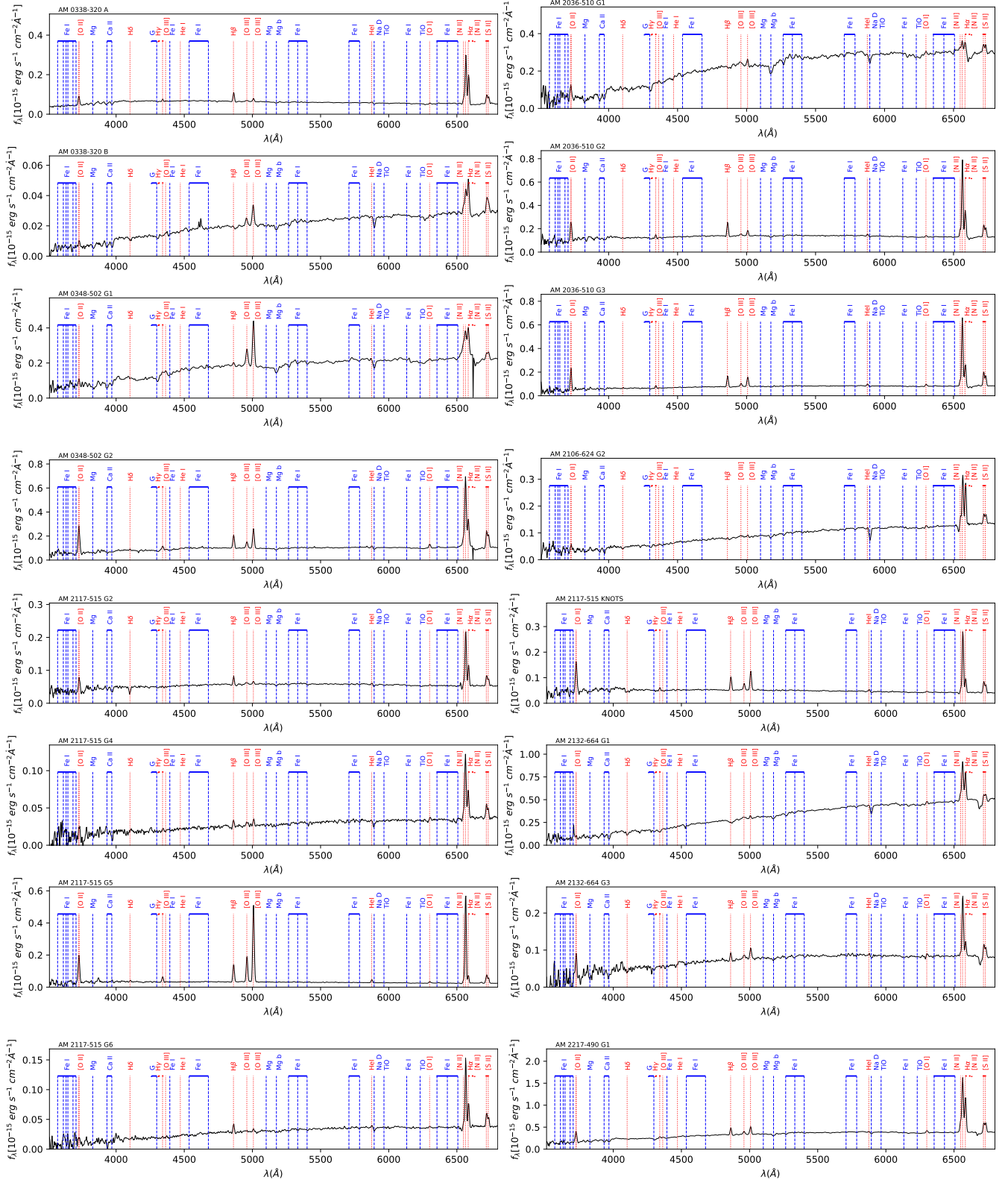


Fig. 2. Examples of nuclear rest-frame spectra (2.2 kpc aperture) of the interacting pairs observed with GMOS-S. The main emission lines and absorption features are indicated as red and blue vertical lines, respectively. The remaining spectra are shown in Fig. A.2 in Appendix A.

(1989). In summary, the adopted ionized gas optical extinction was computed as equation 7 of Riffel et al. (2021). The extinction corrected emission lines fluxes for the INT and CTR galaxies are listed in Tables A.3, A.4, A.5, and A.6 in Appendix A.

3. Stellar populations analysis

Since small differences in the stellar population ages and metallicities are difficult to characterize, to analyse the stellar synthesis output properly, here we use the following binned population

Table 1. Stellar population synthesis main properties derived for the INT and CTR samples. The columns list the mean (\bar{p}), standard deviation (σ), median, and quartile deviation (Q.D) for both samples. The last two columns correspond to the fraction between the median values of the INT and CTR sample and the KS test p-values.

Property	INT (59 galaxies)		CTR (45 galaxies)		INT/CTR	
	$\bar{p} \pm \sigma$	median $\pm Q.D$	$\bar{p} \pm \sigma$	median $\pm Q.D$	Fraction	KS p-value
xy (%)	20 \pm 24	9 \pm 13	10 \pm 9	8 \pm 5	1.11	5.4e-02
xiy (%)	5 \pm 9	0 \pm 4	8 \pm 9	3 \pm 8	0.01	4.5e-02
xio (%)	25 \pm 25	16 \pm 22	14 \pm 13	10 \pm 10	1.63	1.0e-01
$x_{[y,io]}$ (%) ^a	50 \pm 36	55 \pm 35	32 \pm 22	28 \pm 18	1.91	1.2e-03
xo (%)	50 \pm 36	45 \pm 35	68 \pm 22	72 \pm 18	0.64	1.2e-03
$\langle t_* \rangle_L$	9.1 \pm 0.9	9.3 \pm 0.5	9.4 \pm 0.4	9.5 \pm 0.3	0.98	1.5e-02
$\langle Z_* \rangle_L (Z_\odot)$	0.9 \pm 0.3	0.88 \pm 0.19	0.8 \pm 0.2	0.8 \pm 0.1	1.1	4.8e-02
my (%)	1 \pm 4	0.2 \pm 0.6	0.2 \pm 0.5	0.1 \pm 0.1	2.12	1.0e-02
miy (%)	4 \pm 10	0 \pm 1	1 \pm 2	0.5 \pm 0.9	0.02	7.2e-02
mio (%)	24 \pm 30	8 \pm 20	5 \pm 7	2 \pm 3	4.65	1.3e-03
$m_{[y,io]}$ (%) ^a	29 \pm 35	10 \pm 24	6 \pm 8	3 \pm 3	3.02	2.0e-03
mo (%)	71 \pm 35	90 \pm 24	94 \pm 8	97 \pm 3	0.93	2.0e-03
$\langle t_* \rangle_M$	9.7 \pm 0.4	9.9 \pm 0.3	10.0 \pm 0.1	10.01 \pm 0.04	0.99	3.7e-04
$\langle Z_* \rangle_M (Z_\odot)$	0.9 \pm 0.4	0.88 \pm 0.33	0.9 \pm 0.3	0.94 \pm 0.2	0.93	9.7e-02
A_V^* (mag)	1.4 \pm 0.6	1.3 \pm 0.4	0.5 \pm 0.3	0.5 \pm 0.2	2.6	1.0e-12

Notes. ^(a) $x(m)_{[y,io]}$ is the sum of $x(m)y$, $x(m)iy$, and $x(m)io$. This is the sum of the contributions of stellar populations younger than 2 Gyr.

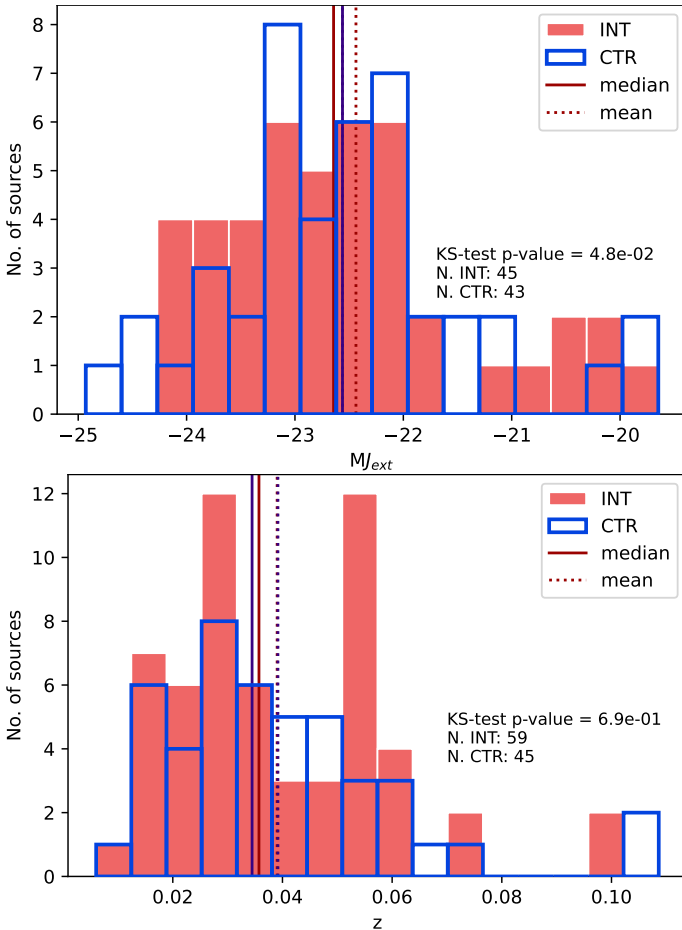


Fig. 3. Distribution of absolute magnitudes (using the available extended J_{ext} 2MASS magnitudes) and redshifts for INT (red filled histograms) and CTR (blue continuous line) samples. The plot also shows the samples median, mean values, and their Kolmogorov-Smirnov (KS) test p-values.

vectors (see Cid Fernandes et al. 2005; Riffel et al. 2009, for more details):

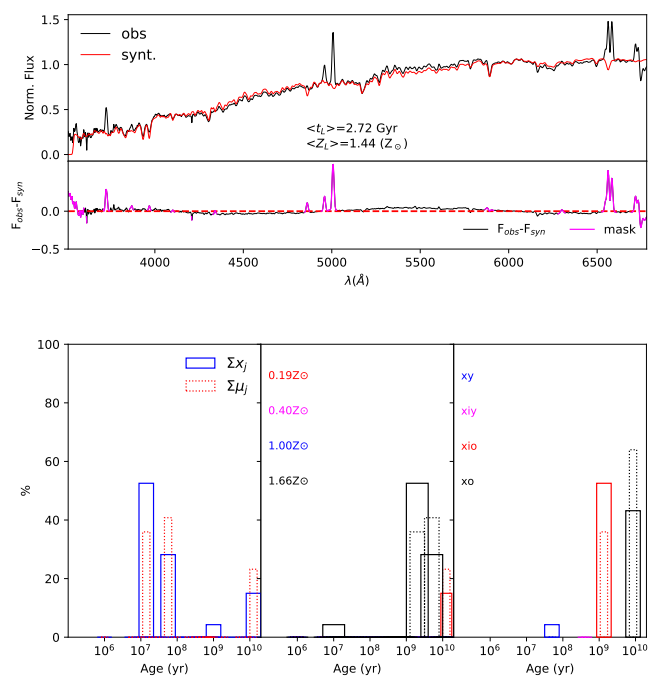


Fig. 4. Example of stellar populations synthesis of AM 1933-422 B. Top panel: Observed and stellar populations synthesis fitting (black and red lines, respectively). The inset at the bottom shows the pure emission line spectra (magenta line). Bottom panel: The left histogram shows, in bins of age, the stellar population contribution in light (solid line) and mass (dashed line) fractions. The middle histogram presents, in bins of age, the metallicity of the fitted stellar populations. The right histogram shows the population vectors in light (solid line) and mass (dashed line) fractions.

xy (my) - young stellar populations: Light (mass) binned population vector in the age range $t \leq 100$ Myr;

xiy (miy) - intermediate young stellar populations: Light (mass) binned population vector in the age range $100 < t \leq 700$ Myr;

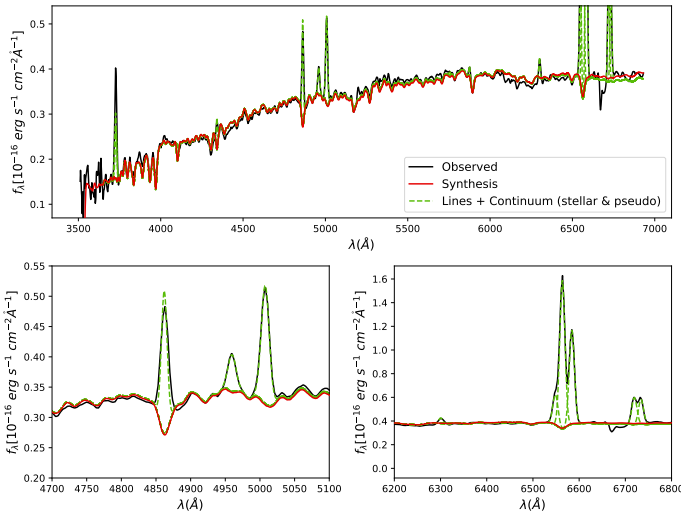


Fig. 5. Example of stellar populations synthesis and emission line fitting for the galaxy AM 22217-490 G1. The modelled emission lines can be seen as dashed green lines and the stellar synthesis as a red line. The bottom left and right panels correspond to the spectral regions around H β and H α , respectively.

xio (mio) - intermediate old stellar populations: Light (mass) binned population vector in the age range 700 Myr < $t \leq 2.0$ Gyr;
 xo (mo) - old stellar populations: Light (mass) binned population vector in the age range 2.0 Gyr < $t \leq 15$ Gyr.

Additionally, following Cid Fernandes et al. (2005), we have also computed the mean logarithm of the ages and the mean metallicities. The mean logarithm of the ages weighted by the stellar light (hereafter light-weighted mean age) and weighted by the stellar mass (hereafter mass-weighted mean age) are defined as follows:

$$\langle t_{\star} \rangle_L = \sum_{j=1}^{N_{\star}} x_j \log t_j, \quad (3)$$

$$\langle t_{\star} \rangle_M = \sum_{j=1}^{N_{\star}} \mu_j \log t_j. \quad (4)$$

Futhermore, the light-weighted and mass-weighted mean metallicities are defined as:

$$\langle Z_{\star} \rangle_L = \sum_{j=1}^{N_{\star}} x_j Z_j, \quad (5)$$

$$\langle Z_{\star} \rangle_M = \sum_{j=1}^{N_{\star}} \mu_j Z_j. \quad (6)$$

Note that the definitions above are limited by the ages and metallicities of our stellar population base, as described in Sect. 2.3.

The results of the stellar populations synthesis modelling are summarized in the histograms shown in Fig. 6 and Table 1. In Table 1, besides presenting the mean and median properties of the INT and CTR samples, we also show the fraction of the medians of the INT and CTR sample and the p-values of corresponding

KS tests. We reject the null hypothesis that the two samples were drawn from the same distribution if the p-value is < 0.01.

The $x_{[y,io]}$ ² and xo histograms in Fig. 6 show a substantial difference between the samples stellar populations. The INT galaxies present higher mean and median contribution from $x_{[y,io]}$ than CTR galaxies, as can be also seen in Table 1. This population dominates ($x_{[y,io]} > 50\%$) in more than half of the INT sample (median INT $x_{[y,io]}$ of $55 \pm 35\%$). The INT median contribution of $x_{[y,io]}$ is nearly twice that of the CTR sample ($28 \pm 18\%$). On the other hand, 3/4 of the CTR sample galaxies are dominated by the old stellar populations (median CTR xo of $72 \pm 18\%$). Furthermore, the INT light-weighted mean ages have a median value of 1 Gyr younger than the CTR sample (see Table 1 and Fig. 6). These findings suggest that the INT sample has a larger content of stellar populations younger than 2 Gyr than the CTR sample.

These differences between the properties of the stellar populations of the INT and CTR samples are also seen in the mass-weighted properties. Table 1 shows that the INT median $m_{[y,io]}$ ³ is more than three times the CTR, albeit with a large scatter. This result is mainly driven by the intermediate old population (mio), which exhibits an INT median mass fraction contribution nearly five times higher than in the CTR. Consequently, the INT mass-weighted mean ages show a median value 2 Gyr younger than the CTR sample.

The samples also show differences in the mean stellar metallicities of the stellar populations. As seen in Fig. 6 and Table 1, the light-weighted mean metallicities present similar distributions, with the INT sample presenting a slightly higher median value than the CTR. When considering the mass-weight mean metallicities, the opposite occurs, with the INT median value being smaller than that of the CTR sample. According to the KS test however, we cannot rule out that they come from the same distribution.

The property that more clearly distinguishes the samples is the stellar extinction (A_V^*). Fig. 6 and Table 1 show that the INT sample distribution is shifted towards high A_V^* values compared to the CTR sample. The median INT sample A_V^* is 2.6 times higher than in the CTR. Besides the higher mean and median values, the KS test confirms that the distributions are unlikely to come from the same initial one.

As seen in Table 1 and Fig. 6, the INT sample often presents much wider distributions (greater standard and quartile deviations⁴) in stellar populations properties compared to the CTR sample, showing that the INT galaxies span a wider range of stellar population properties.

Finally, we did the test of analysing the stellar population properties by removing the 14 INT galaxies without a CTR (see Section 2.2 for more details on the CTR sample selection), and found no significant changes in the overall distributions, median, and mean values.

4. Reddening effects

In the left panel of Fig. 7 we present the A_V^{gas} distribution, which is the reddening obtained via the H α over H β emission line flux

² $x_{[y,io]} = xy + xi y + xio$. The $x_{[y,io]}$ is the sum of light-fraction contributions of stellar populations younger than 2 Gyr.

³ $m_{[y,io]} = my + mi y + mio$. The $m_{[y,io]}$ is the sum of mass-fraction contributions of stellar populations younger than 2 Gyr.

⁴ The quartile deviation is defined as half of the interquartile range (IQR), used as a measure of the dispersion for median values (Kenney 1939).

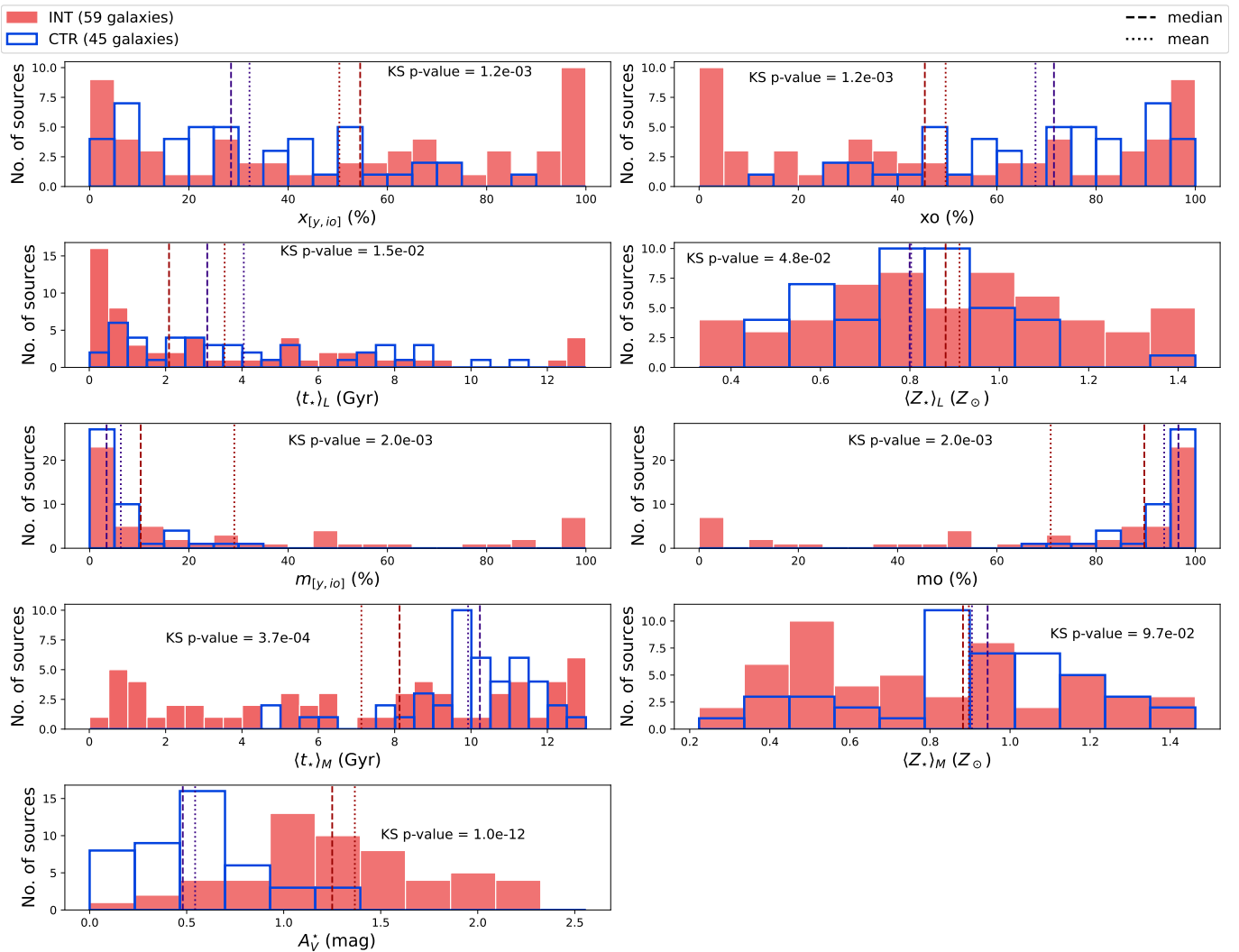


Fig. 6. Histograms of the stellar populations synthesis modelling for INT (filled red bars) and CTR (full blue lines) samples. The histograms also show the mean (dotted vertical lines) and median (dashed vertical lines) values for both samples and the KS test p-value. The first two rows of histograms present the light-weighted properties. They present the sum of light fractions younger than 2 Gyr ($x_{[y,io]} = xy + x_{iy} + x_{io}$), the light fractions in the older stellar populations (xo), the light-weighted mean ages, and mean metallicities. The following two rows present the mass-weighted results of the same properties. The lower right histogram shows the stellar extinction of the samples.

Table 2. Ionized gas and stellar extinction properties of the INT and CTR samples. The measurements were computed for galaxies where an extinction calculation was possible. The columns include the mean (\bar{p}), standard deviation (σ), median, and quartile deviation (Q.D.) for both the INT and CTR samples. The last two columns correspond to the fraction between the median values of the INT and CTR sample and the KS test p-values.

Property	INT (50 galaxies)		CTR (40 galaxies)		INT/CTR	
	$\bar{p} \pm \sigma$	median $\pm Q.D.$	$\bar{p} \pm \sigma$	median $\pm Q.D.$	Fraction	KS p-value
A_{Vgas} (mag)	3 ± 1	3.0 ± 0.8	1.6 ± 0.8	1.5 ± 0.4	1.91	$3.5e-07$
A_{Vgas}/A_{V^*}	2 ± 1	2.0 ± 0.9	3 ± 3	2.5 ± 0.7	0.8	$4.4e-02$

ratios. As shown in Table 2, the nebular extinction of the INT sample has higher mean and median values than the CTR. The median ionized gas extinction of the INT sample (median \pm Q.D. = 3.0 ± 0.8 mag) is nearly twice the one on the CTR sample (median \pm Q.D. = 1.5 ± 0.4 mag). The KS test p-value suggests that the samples are unlikely to come from the same original distribution.

On the right panel of Fig. 7, we show A_V^{gas} vs A_V^* plot. The INT sample presents a higher dispersion on both extinctions than the CTR. Consequently, the CTR shows a stronger correlation between the two quantities than the INT galaxies. Some INT

galaxies appear to be offset towards high A_V^* and closer to the 1:1 relation. This could suggest that some of these galaxies have a significant fraction of stars in more gas-rich and star-forming regions. This will be further explored in Sec. 7.2.

5. Excitation mechanisms

Emission-line diagnostic diagrams are essential tools used to characterize the main ionization mechanisms of the gas. We applied them to compare the sources of ionization that drive the emission on the INT and CTR samples. Figure 8 presents the

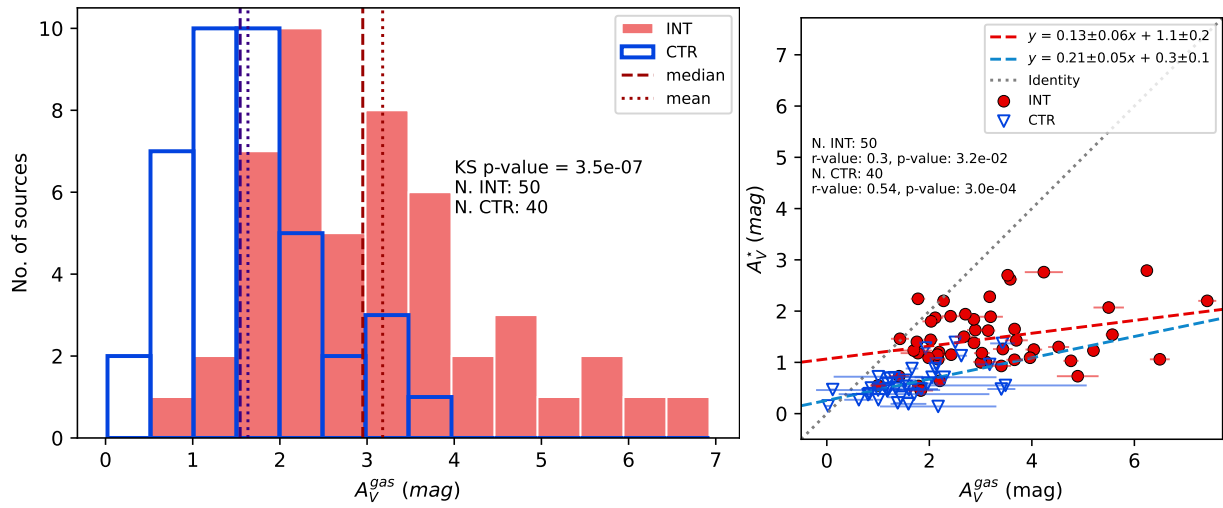


Fig. 7. Left-panel: Histogram of the gas extinction obtained via Balmer decrement for the INT (in red) and CTR sample galaxies (in blue). The mean and median values of both samples as in Fig. 11. Right-panel: Relation between stellar extinction (A_V^*) and nebular extinction (A_V^{gas}) for the INT (red circles) and CTR (blue triangles) samples. Dashed lines show the best linear regression fit obtained in both cases. The linear equations, Pearson correlation coefficients (r-value) and p-values of the fits are indicated in the inset. The grey dotted line corresponds to the case when $A_V^{gas} = A_V^*$.

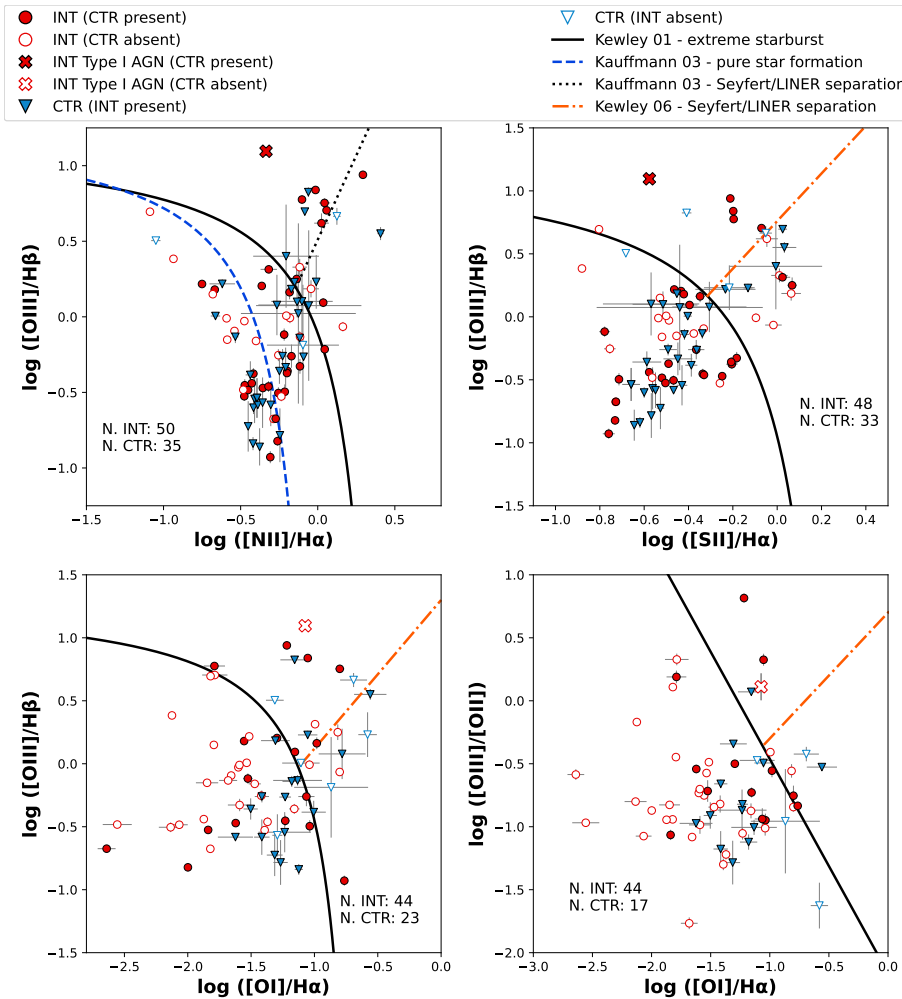


Fig. 8. Emission-line diagnostic diagrams used to compare the ionization mechanisms of the INT galaxies (red points) and the CTR sample (blue triangles). Filled symbols correspond to INT (CTR) galaxies whose corresponding CTR (INT) galaxy is also included on that diagram, and open symbols when it is not. Lines in the diagrams represent the theoretical (Kewley et al. 2001) and empirical (Kauffmann et al. 2003; Kewley et al. 2006) divisions applied in this work to classify the ionization sources. Each diagram shows the number of sources included in each diagram. The red cross marks the position on the diagrams of the only type I AGN found in the INT sample.

traditional BPT diagram (hereafter, [NII] BPT), followed by the diagrams involving [SII] $\lambda\lambda$ 6717, 6731 Å (hereafter, [SII] BPT), [OI] λ 6300 Å (hereafter, [OI] BPT) and [OII] $\lambda\lambda$ 3727, 3729 Å (hereafter, [OII] BPT) (Baldwin et al. 1981; Veilleux & Osterbrock 1987). We also use the WHAN diagram (Cid Fernandes et al. 2010, 2011) presented in Fig. 9. In all the diagrams, we plot empirical and theoretical curves (Kewley et al. 2001; Kauffmann et al. 2003; Kewley et al. 2006; Stasińska et al. 2006; Cid Fernandes et al. 2011) to enable us to classify the main sources of ionization, which is indicated in Tables A.7 and A.8 in Appendix A.

In Fig. 10, we show the histograms with the fractions of activity type classification derived from the diagrams in Figs. 8 and 9. In all diagrams of Fig. 8, the fraction of galaxies for which we could not measure one or more emission lines is higher in the CTR sample. On the BPT diagram, 22% (10/45 sources) of CTR galaxies were not classified, against 15% (9/59 sources) of the INT sample. A similar fraction was found on the [SII] BPT. In the last two diagrams, the absence of classification is higher. The CTR galaxies present a fraction of 49% (22/45 objects) and 62% (28/45 objects) of galaxies unclassified in the [OI] BPT and [OII] BPT, respectively. On the same diagrams, the fraction of INT galaxies that are not classified are 25% in both (15/59 sources).

The WHAN diagram, which includes a higher number of CTR galaxies than the BPTs since several galaxies with H α equivalent width (EW) $< 3 \text{ \AA}$ may lack the other emission lines involved in the latter, suggests an excess of retired galaxies in the CTR sample, as seen in Figs. 9 and 10. In this diagram, 33% (15/45 galaxies) of the CTR sources were classified as retired, while in the INT sample the fraction was 22% (13/59 galaxies).

The histograms of Fig. 10 show that more INT galaxies are classified as star-forming than in the CTR. In the BPTs and WHAN diagrams, between 27–59% (16–35/59 galaxies) of the INT sample are classified as star-forming, whilst in the case of the CTR sample, they represent between 20–55% (9–25/45 sources). The difference is more evident in the [OI] and [OII] BPT diagrams, where 54% and 63% (32 and 37 out of 59 galaxies) of the INT sample, respectively, are classified as star-forming versus 33% and 31% (15 and 14 out of 45 galaxies) of them in the CTR sample. Our findings suggest that interactions may be responsible for the enhancement in star formation in the INT sample.

When considering the AGN classification in Fig. 10, the Seyfert or strong AGN (sAGN) classification of the INT sources outnumbers the CTR ones in all five diagrams. The diagrams with the highest excess are the [NII] BPT and WHAN, where the INT sample contains 14–39% (8–23/59 sources) of AGN, respectively, versus 9–29% (4–13/45 galaxies) of the CTR sample. Although the difference in the fraction of AGN is small, it indicates that nuclear activity might be enhanced due to galaxy interactions in the INT sample.

To find a consensus about the dominant source of ionization of the central region of the INT and CTR galaxies, all five diagrams were combined on the bottom right histogram of Fig. 10. This final classification was done by considering only galaxies with consistent classification in at least four out of the five diagrams. Then, these galaxies were classified into one of the following groups:

1. Star-forming (SF): Galaxies classified as star-forming.
2. Retired galaxies (RG): Galaxies classified as retired in the WHAN diagram and as LINER in at least three BPT diagrams.

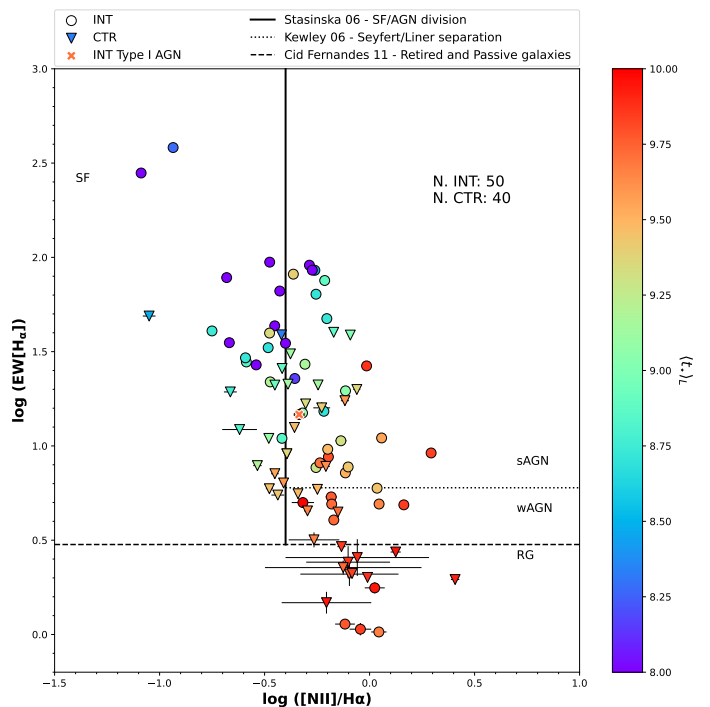


Fig. 9. The diagram of [NII]/H α versus the equivalent width of H α (WHAN diagram, Cid Fernandes et al. 2010, 2011). INT galaxies are shown as circles, and CTR galaxies are shown as triangles. Symbol colours indicate the light-weighted mean ages of the stellar populations, showing the youngest mean ages in the star-forming galaxies and the oldest in the retired galaxies. Lines represent the divisions applied in this work to obtain the sources of ionization (Stasińska et al. 2006; Kewley et al. 2006; Cid Fernandes et al. 2011). The cross marks the position on the diagram of the only type I AGN found in the INT sample.

3. AGN: Galaxies classified as LINER, Seyfert, wAGN, sAGN or composite.

It is important to note that this is a conservative approach since we require the same classification in four out of five diagrams to classify a galaxy as SF, RG, or AGN. The remaining galaxies are classified as inconclusive (INC) in the bottom right histogram of Fig. 10. As can be seen in the first rows of Table 3, we find that 47% (28/59 objects) of the INT sample and 24% (11/45 galaxies) of the CTR sample could be included in each of the three categories listed above. Only one RG galaxy was consistently found in the CTR sample. 34% (20/59 sources) of the INT sample and 16% (7/45 objects) of the CTR sample were consistently classified as SF. These results suggest that, even after using our restrictive criteria, there is an excess of 18% of SF galaxies in the INT sample relative to the CTR sample. Regarding the AGN classification, we found that they are more common in the INT sample (8/59 sources, 14%) than in the CTR sample (3/45 sources, 7%).

Relaxing our criteria can reduce the number of galaxies without classification and increase the number of galaxies in both the INT and CTR samples. Table 3 presents the consistent classifications found using three out of the five diagrams (3/5 DGs), [NII] and [SII] BPTs combined to the WHAN diagram ([NII]+[SII]+WHAN), and [NII] BPT with WHAN diagram ([NII]+WHAN). We were able to find a classification for up to 78% (46/59 galaxies) of the INT sources and 51% (23/45 galaxies) of the CTR sources. We find that the INT sample has between 1.4 to 2.2 times higher fraction of star-forming galaxies than the CTR sample (0.9 to 1.7 if we exclude the 14 INT galax-

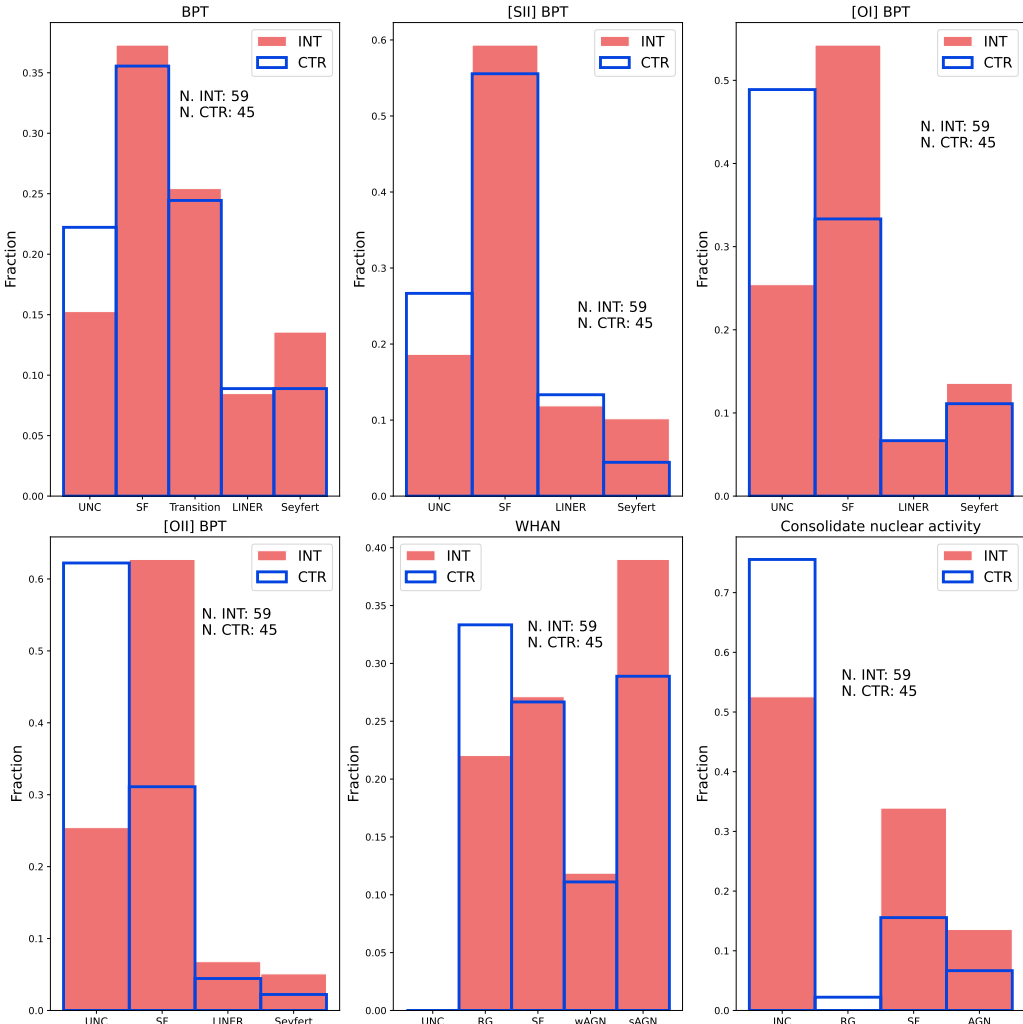


Fig. 10. Histograms of the dominant gas ionization mechanisms found from each diagnostic diagram. The three top and the bottom left histograms show the fractions of galaxies classified from the BPT diagrams as star-forming (SF), AGN (LINER or Seyfert) and composite ([NII] BPT). For the WHAN diagram, the galaxies are classified as retired (RG), SF, strong-AGN (sAGN), and weak-AGN (wAGN). Galaxies that could not be classified in a particular diagram are shown in the histograms as unclassified. The bottom right histogram summarizes the information obtained from all the diagrams, which we divided into four categories: SF, AGN, RG, and inconclusive (INC). Galaxies included in the SF, AGN, and RG groups are those having the same classification on at least four out of the five BPT and WHAN diagrams.

ies without CTR galaxies). The fraction of AGN in the INT sample is between 2 and 3.4 times greater than the CTR sample (2.3 to 4 if we exclude the 14 INT galaxies without CTR galaxies). Although the fractions change with the criteria and depending on whether we consider INT galaxies with controls or not, we always obtain an excess of AGN galaxies in the INT sample relative to the CTR sample, showing the reliability of this result.

In order to further test how strong the previous results are, we only considered INT galaxies whose CTR is also classified in the same diagram(s). This has the problem that the number of galaxies is then reduced (between 4 and 19 in the four combinations of diagrams reported in Table 3). By doing this, we measure a fraction of AGN between 1.6 and 2.3 times greater in the INT sample than the CTR sample, confirming the previous result. However, for the fraction of SF the trend reverts, and we find between 1.2 and 1.4 times higher fraction in the CTR sample than in the INT sample. Therefore, based on the analysis done here, we conclude that the number of AGN in the interacting galaxies is larger than in the non-interacting ones, while for the SF galaxies we cannot either confirm or discard any trend.

6. Do interactions enhance star-formation?

To evaluate the strength of star formation in both samples, here we consider the INT and CTR sample galaxies classified as SF in the bottom right histogram of Fig. 10 (34% of the INT and 16% of the CTR sample).

The histogram on the left panel of Fig. 11 shows the distribution of EW(H α), of the SF galaxies and Table 4 summarizes their star formation properties. SF galaxies in the INT sample have significantly higher EW(H α) values (median \pm QD. = $40 \pm 28 \text{ \AA}$) compared to the SF CTR sample (median \pm QD. = $19 \pm 4 \text{ \AA}$). This result suggests the presence of younger stellar populations photoionizing the gas and contributing to this enhancement of EW(H α) in the INT systems when compared with CTR ones.

In the right panel of Fig. 11, we combine the stellar population synthesis modelling results with EW(H α). Only SF INT galaxies exhibit light-weighted mean stellar ages younger than 100 Myr and EW(H α) $> 50 \text{ \AA}$. Furthermore, as shown in Table 4, the light-weighted mean stellar ages of SF INT galaxies have a median value of 100 Myr, while the SF CTR galaxies exhibit a median value of 1.2 Gyr. The fit of the SF INT galaxies

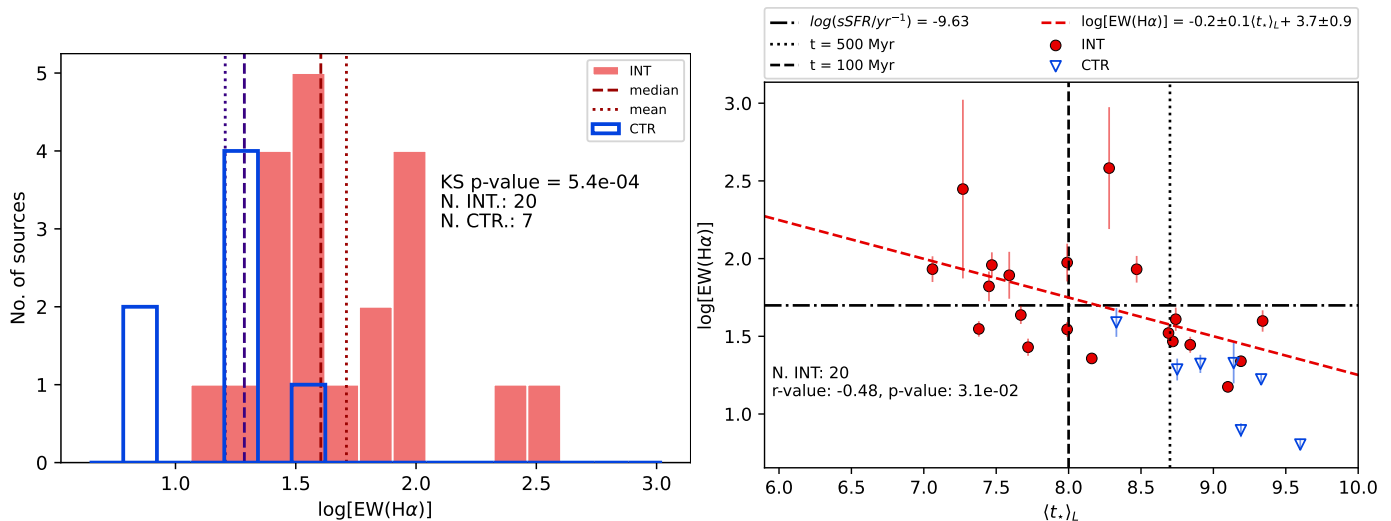


Fig. 11. Left panel: Distribution of $\text{EW}(\text{H}\alpha)$ for the bona-fide SF galaxies. Right panel: The relation between light-weighted mean ages $\langle t_* \rangle_L$ and $\text{H}\alpha$ equivalent width for SF galaxies. SF INT galaxies are shown as red circles, and the SF CTR as blue triangles. The red dashed line corresponds to the linear regression fit obtained for the SF INT galaxies. The linear equation, Pearson correlation coefficient (r -value), and p -value of the fit are provided in the inset. The black dashed and dotted lines indicate the mean stellar ages of 100 Myr and 500 Myr, respectively. The dot-dashed line indicates an $\text{EW}(\text{H}\alpha) = 50 \text{ Å}$ or $\log(\text{sSFR}/\text{yr}^{-1}) = -9.63$.

Table 3. The classification of the galaxies in the INT and CTR samples using four distinct combinations of diagnostic diagrams. The INT and CTR columns include the percentual and the number of galaxies between parentheses.

Properties	% INT (N gal.)	% CTR (N gal.)	% INT/% CTR
4/5 DGs^a			
INC	53 (31)	76 (34)	0.7
RG	0 (0)	2 (1)	0.0
SF	34 (20)	16 (7)	2.18
AGN	14 (8)	7 (3)	2.03
3/5 DGs^b			
INC	22 (13)	49 (22)	0.45
RG	2 (1)	7 (3)	0.25
SF	54 (32)	38 (17)	1.44
AGN	22 (13)	7 (3)	3.31
[NII] + [SII]+WHAN^c			
INC	58 (34)	73 (33)	0.79
RG	2 (1)	4 (2)	0.38
SF	25 (15)	18 (8)	1.43
AGN	15 (9)	4 (2)	3.43
[NII]+WHAN^d			
INC	31 (18)	51 (23)	0.6
RG	2 (1)	9 (4)	0.19
SF	27 (16)	20 (9)	1.36
AGN	41 (24)	20 (9)	2.03

Notes. All the classifications require agreement in: ^(a) at least four out of the five diagnostic diagrams ^(b) at least three out of the five diagnostic diagrams ^(c) the [NII], [SII], and WHAN diagrams ^(d) the [NII] BPT and WHAN diagrams.

shown in the right panel of Fig. 11 suggests an anti-correlation (Pearson $r = -0.48$), which is expected if there is a connection between the enhancement of $\text{EW}(\text{H}\alpha)$ and the age of the stellar populations.

We can use $\text{EW}(\text{H}\alpha)$ to estimate the specific star formation rate ($\text{sSFR} = \text{SFR}/M_\star$). Using equation $\log(\text{sSFR}/\text{yr}^{-1}) = -11.87 + 1.32 \log(\text{EW}(\text{H}\alpha))$ from Belfiore et al. (2018), we found, as shown in Table 4, that SF INT galaxies have median sSFR 2.6 times higher than SF CTR galaxies. At this rate, SF INT galaxies will need less than half of the time of SF CTR galaxies to double their stellar mass. We also calculated the sSFR

(see Table 4) from the stellar populations modelling, using the $\text{SFR}^{20\text{Myr}}\text{⁵}$, and found similar results as with $\text{EW}(\text{H}\alpha)$.

7. Discussion

7.1. The stellar populations and recent star formation of interacting galaxies

It is well-known that interactions and mergers can induce star formation (Sanders & Mirabel 1996; Ellison et al. 2013; Knapen et al. 2015; Krabbe et al. 2017). We used stellar population synthesis modelling to confirm or discard the presence of recent star formation in our samples. Our findings reveal that more than half of the INT sample is dominated (see Table 1) by stellar populations younger than 2 Gyr (i.e., higher light-weighted fractions). The median contribution from these young stellar populations in the INT sample is nearly 2 times that of the CTR sample. This difference between the stellar populations of the INT and CTR samples is also detected in the mass-weighted fractions.

Regarding the stellar populations light-weighted stellar population fractions, our results agree with the findings of previous studies, mostly done in small samples or individual pairs. For instance, Krabbe et al. (2017) analysed 15 galaxies in 9 close pairs using long-slit spectroscopy. They also used STARLIGHT but with BC03 models (Bruzual & Charlot 2003). In agreement with our findings, the stellar population synthesis modelling revealed that 11 out of the 15 galaxies in their sample were dominated in light fractions by young to intermediate stellar populations (< 2 Gyr).

Bessiere et al. (2017) presented optical spectroscopy observations of 21 type-II quasars. Their study investigates the time scales of starburst and AGN triggering associated with merger events. They built stellar population models with STARBURST99 (Leitherer et al. 1999) and fitted the spectra using the routine CONFIT (Robinson et al. 2000). For most quasars, they were able to fit an 8 Gyr plus a young stellar population (YSP). They found YSP light fractions between 15%-100% and maximum YSP ages below 200 Myr. These fractions are much greater than

⁵ The star-formation rate over the last 20 Myr ($\text{SFR}^{20\text{Myr}}$) was calculated following Riffel et al. (2021, 2023).

Table 4. Ionized gas and stellar population properties of SF galaxies of the INT and CTR samples, as classified in Sec. 5. The columns include the mean (\bar{p}), standard deviation (σ), median, and quartile deviation (Q.D) for both the INT and CTR samples. The last two columns correspond to the fraction between the median values of the INT and CTR sample and the KS test p-values.

Property	SF INT (20 galaxies)		SF CTR (7 galaxies)		INT/CTR	
	$\bar{p} \pm \sigma$	$median \pm Q.D$	$\bar{p} \pm \sigma$	$median \pm Q.D$	Fraction	KS p-value
Ionized gas						
EW(H α) (\AA)	77 \pm 90	40 \pm 28	19 \pm 10	19 \pm 4	2.08	5.4e-04
log(sSFR/yr $^{-1}$) ^a	-9.6 \pm 0.5	-9.8 \pm 0.3	-10.3 \pm 0.3	-10.2 \pm 0.2	0.96	5.4e-04
sSFR (yr $^{-1}$) ^a	5e-10 \pm 8e-10	2e-10 \pm 2e-10	7e-11 \pm 5e-11	7e-11 \pm 2e-11	2.63	5.4e-04
1/sSFR (Gyr) ^a	6 \pm 5	6 \pm 3	26 \pm 20	15 \pm 10	0.38	5.4e-04
Stellar population modelling						
$\langle t_{\star} \rangle_L^b$	8.2 \pm 0.7	8.0 \pm 0.6	9.0 \pm 0.4	9.1 \pm 0.2	0.88	1.2e-02
SFR $^{20\text{Myr}}$ (M $_{\odot}$ /yr) ^b	3 \pm 4	2 \pm 1	0.6 \pm 0.6	0.3 \pm 0.4	4.85	6.3e-02
log(sSFR $^{20\text{Myr}}$ /yr $^{-1}$) ^b	-9.3 \pm 0.6	-9.2 \pm 0.5	-10.0 \pm 0.4	-10.0 \pm 0.3	0.92	1.6e-02
sSFR $^{20\text{Myr}}$ (yr $^{-1}$) ^b	1e-09 \pm 1e-09	6e-10 \pm 8e-10	1e-10 \pm 1e-10	9e-11 \pm 8e-11	6.55	1.6e-02
1/sSFR $^{20\text{Myr}}$ (Gyr) ^b	4 \pm 5	2 \pm 2	13 \pm 10	11 \pm 7	0.15	1.6e-02

Notes. ^(a) The specific star formation rate (sSFR) was obtained from the equation $\log(\text{sSFR}/\text{yr}^{-1}) = -11.87 + 1.32 \log(\text{EW(H}\alpha\text{)})$ from [Belfiore et al. \(2018\)](#).

^(b) These properties were obtained from the stellar population synthesis modelling. The star-formation rate over the last 20 Myr (SFR $^{20\text{Myr}}$) was calculated following [Riffel et al. \(2021, 2023\)](#).

the median values found in our INT sample for our youngest stellar populations. Despite the different models and fitting procedures, most of their quasars are in a later stage in the merging process, and have larger gas masses, both having an impact on star formation.

We also analysed the star formation enhancement using nebular indicators. Since the H α equivalent width is a stellar age indicator in HII regions ([Copetti et al. 1986; Kennicutt 1998; Kennicutt & Evans 2012; Tacconi et al. 2020; Sánchez 2020; Sánchez et al. 2021](#)) and it is used as a proxy to derive the sSFR, we used it to compare the bona-fide star-forming galaxies in our INT and CTR samples. As shown in Table 4, the median EW(H α) for SF INT galaxies is 2 times higher than for the CTR sample. Higher equivalent widths in interacting systems were also found in [Donzelli & Pastoriza \(1997\)](#). The authors analysed the spectra of 27 galaxies in pairs and found mean values of the equivalent width of H α +[NII] ranging from 37-54 \AA against a mean of 27 \AA in visual pairs (i.e., discarded as pairs spectroscopically).

From EW(H α) we measure a median sSFR of the SF INT galaxies 2.6 times higher than that of the SF CTR galaxies, which means that at this star formation rate, SF INT galaxies will need less than half of the time of SF CTR galaxies to double their stellar mass. The sSFRs values obtained here are compatible with the ones found in interacting gas-rich spiral galaxies in [Knapen et al. \(2015\)](#). In that work, the authors analysed 1500 nearby interacting galaxies using estimates of SFR and sSFR from [Querejeta et al. \(2015\)](#) based on far-infrared emission and selected a control sample of isolated galaxies with similar masses and morphologies. They found that the interacting galaxies have SFRs and sSFRs up to twice higher than those measured for the control sample. [Hwang et al. \(2011\)](#) also studied the sSFR in interacting galaxies and found an enhancement in spiral pairs. They found the sSFR to be 1.8 up to 4.0 times higher than in non-interacting galaxies. Their sSFRs are similar to the ones from our work.

7.2. Stellar and nebular reddening.

The analysis of the stellar and ionized gas extinction revealed that the INT sample presents higher median stellar and ionized

gas reddening (1.3 ± 0.4 mag and 3 ± 1 mag) than the CTR sample (0.5 ± 0.2 mag and 1.5 ± 0.4 mag, see Tables 1 and 2). These results are in agreement with the previous ones that found that the line-emitting gas is in dustier regions than the stars ([Calzetti et al. 1994; Asari et al. 2007; Riffel et al. 2008, 2009, 2021, 2023; Martins et al. 2013; Dametto et al. 2014; Krabbe et al. 2017](#)).

[Calzetti et al. \(1994\)](#) interpreted this result as due to the fact that the ionized gas is more often associated with dust than the old stellar populations that largely contribute to the stellar continuum. The extinction ratios (see Table 2) are consistent with those reported in the literature for star-forming ([Calzetti et al. 1994; Asari et al. 2007; Riffel et al. 2008](#)) and AGN ([Riffel et al. 2021](#)) galaxies, which often report nebular extinctions around twice the stellar. The same was found in interacting pairs ([Krabbe et al. 2017](#)).

The interacting galaxies in our sample exhibit higher median stellar and emission-line gas reddening relative to control galaxies. This result suggests that the interacting galaxies are more frequently dustier. This result agrees with [Yuan et al. \(2012, see also Hwang et al. 2011 for more details on the effect of interactions in dust properties.\)](#) that analyzing GALEX ultraviolet and Spitzer infrared data, found that interacting galaxies, especially spiral pairs, present higher dust attenuation than isolated galaxies. This is also predicted from simulations (e.g.; [Yutani et al. 2022](#)) where an increase of dust in the central regions of interacting galaxies could, in the late stages of the merging process, lead to dust-obscured galaxies (DOGs).

Some interacting galaxies in our sample were found closer to the $A_V^{\text{gas}} = A_V^{\star}$ relation shown in Fig. 7 than others. This could indicate that the stellar populations there are associated with dusty star-forming regions. To confirm this hypothesis, in Fig. 12 we show the relation between the stellar and emission line extinctions in the INT sample, with colours indicating the light-weighted mean ages. The interacting galaxies above the linear fit have median light-weighted mean age of 220 ± 870 Myr (the median value is 3.1 ± 2.3 Gyr in the INT galaxies below the linear fit) meaning that they have a high amount of very hot massive stars. We checked if the distance between the points in Fig. 12 and the 1:1 relation correlates with their light-weighted mean stellar ages, but we did not find any correlation.

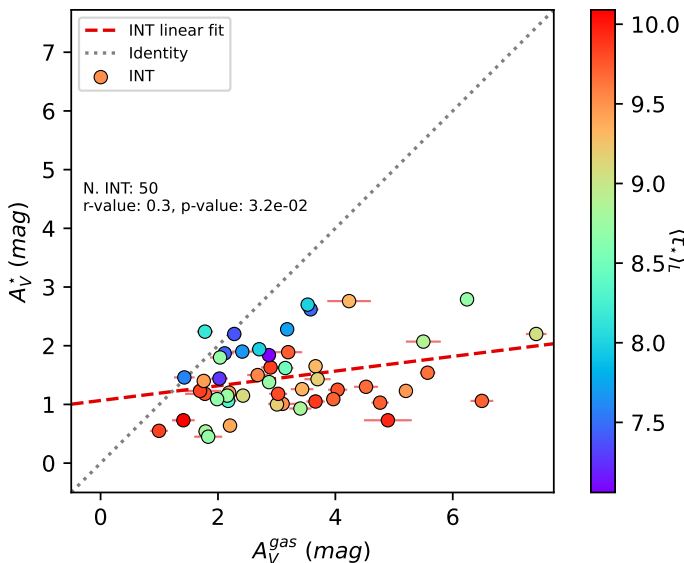


Fig. 12. Relation between A_V^{gas} versus A_V^* for the INT sample. The colors indicate the light-weighted mean ages of the stellar populations. As in Fig. 7, the plot also includes the linear fit for the INT sample and the 1:1 relation.

7.3. Triggering of nuclear activity and star formation in interacting galaxies.

In our analysis of the main sources of ionization, five different diagnostic diagrams were applied (see Sec. 5). We combine the results of the five diagnostics and require agreement in their classification on at least four diagrams for the sources to be classified as star-forming (SF), retired galaxies (RG), and AGN. Because of the lack of information in some diagnostics, combined with the inconsistencies between the classifications, it was not possible to classify the dominant ionization mechanism for 34 galaxies (76%) in the CTR sample and 31 galaxies (53%) in the INT sample. Considering the galaxies that we could classify, we measure 34% of SF, 14% of AGN, and 0% RGs in the INT sample and 16% of SF, 7% of AGN, and 2% of RGs in the CTR sample.

There are similar works in the literature addressing the classification of galaxies in terms of the dominant ionizing source using optical diagnostic diagrams using large survey data, such as the SDSS-III (York et al. 2000; Eisenstein et al. 2011) and the SDSS-IV integral field spectroscopy (hereafter IFS) survey of Mapping Nearby Galaxies at Apache Point Observatory (MaNGA, Bundy et al. 2015). It is not straightforward to compare with these works since they differ in sample and control sample selection, pair mass ratio and mergers stages, redshifts and analysis methods. Nevertheless, in the next paragraphs, we try to compare our findings with some studies.

Sabater et al. (2013) studied the dependence of the dominant ionizing source of the gas on the environment and interactions using single fiber observations of a sample of 270.000 galaxies from SDSS-III. The authors used the traditional [NII] BPT diagram to classify their sources and applied a cut on [OIII] luminosity to classify the passive galaxies. They found that the incidence of galaxy interactions decreases from star-forming galaxies to Seyferts to LINERs to passive galaxies.

Ellison et al. (2013) presented a study of 10.800 close pairs and 97 post-mergers using single fiber observations from the SDSS-III. A control sample of isolated galaxies was selected, taking control of the redshift, mass, and density of the environment. As in the previous case, the study used the [NII] BPT dia-

gram, considering as AGN just Seyfert and composite galaxies. They found fractions of star-forming galaxies of 20% in close pairs (8% in the controls) and 40% in post-merger stages (14% in their controls). They calculated the ratio between the fractions found in the two samples and found that their interacting galaxies present a factor $\sim 2\text{-}3$ higher in star-forming galaxies relative to their controls. The authors also found an increasing AGN excess with decreasing pair separation, presenting a fraction of 2.5 times more AGN in close pairs and 3.75 in post-mergers relative to the control galaxies.

Jin et al. (2021) selected a sample of 1156 galaxies in pairs and 2317 isolated galaxies from the SDSS-IV MaNGA survey. They separated the interacting galaxies in different stages of the merging process and used the [NII] and [SII] BPTs. They used the WHAN diagram only for removing the retired galaxies from their samples. Galaxies were classified as AGN if they fell in the Seyfert or LINER regions of either of the BPT diagrams. They reported 5.5% of AGN, 6.6% of composite galaxies, 27.8% of SF, 28.1% of RGs, and 32% of lineless galaxies in the sample of pairs. For the controls, they find 5% of AGN, 10.2% of composite galaxies, 42.3% of SF, 26.7% of RG and 15.8% of lineless galaxies. The authors argue that they found no significant AGN excess in the pairs compared to the controls. In close pairs in strong interactions, however, they reported a fraction of 19.5% (AGN + composite) against 15.2% in the isolated sample.

Steffen et al. (2023) used the last SDSS-IV MaNGA data release and found 391 pairs (213 minor and 178 major mergers). The control sample was built from 7811 MaNGA galaxies without companions with $\Delta v < 2000$ km/s. The dominant ionization source was classified based on the [NII] BPT and on the WHAN diagram to remove the retired galaxies but with a more restricted cutoff in $\text{EW}(\text{H}\alpha)$ of 6 Å. The galaxy pairs exhibit 13.4% of AGN (62 composites, 18 LINERs, and 25 Seyferts) versus 11.1% in their control sample (613 composites, 70 LINERs, 126 Seyferts, and 63 broad line AGN).

In our work, we find that the INT sample has between 1.4 and 2.2 times higher fraction of star-forming galaxies than the controls, depending on the diagnostic diagrams used to classify the galaxies as star-forming (see Section 5). These fractions are compatible with those reported by Ellison et al. (2013). However, this excess of SF galaxies in the INT sample decreases when we exclude the 14 INT galaxies without controls (fractions from 0.9 to 1.7) and it becomes a deficit if we only consider INT (CTR) galaxies with having their twin CTR (INT) galaxy classified in the same diagram (between 1.2 and 1.4 times higher fractions of SF galaxies in the CTR than in the INT sample).

Considering the bona-fide AGN that we classified here (including LINER/wAGN, Seyfert/sAGN and Composite galaxies), we found a fraction of 14% (8/59 objects). This is similar to the fractions reported in the works by Jin et al. (2021) (AGN + transition galaxies: 12%) and Steffen et al. (2023) (13%). Using different diagnostic diagrams (BPTs and WHAN) we find between 2 and 3.4 times more AGN in the INT sample than in the CTR sample, which agrees with the factor of 2.5 reported by Ellison et al. (2013) for close pairs. Even when we restrict the sample to include 1) only INT galaxies with CTR and 2) INT (CTR) galaxies having their twin CTR (INT) galaxy classified in the same diagram, we still find a higher fraction of AGN in the INT sample relative to the CTR sample, ranging from 1.6 to 4.

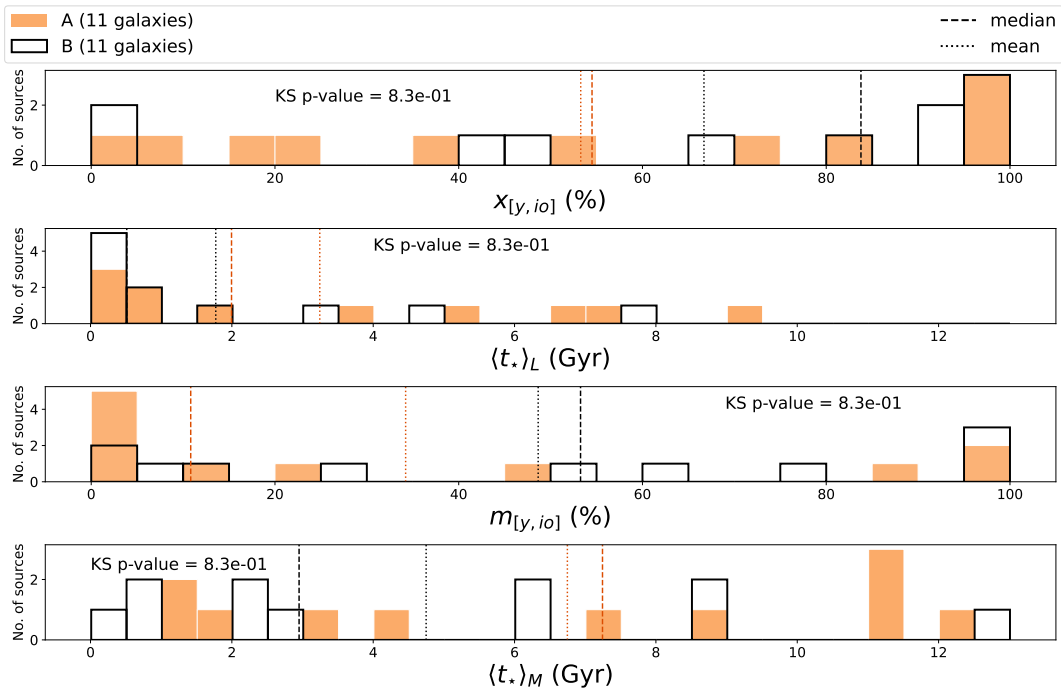


Fig. 13. Histograms of the light and mass fractions younger than 2 Gyr ($x_{[y,io]}$ and $m_{[y,io]}$) and light- and mass-weighted mean stellar ages ($\langle t_* \rangle_L$ and $\langle t_* \rangle_M$) of the A (filled histograms) and B members (empty histograms) of INT pairs with $M[A] > 2M[B]$. The histograms also show the mean (dotted vertical lines), median (dashed vertical lines), and KS p-values.

7.4. Interacting pairs properties

Many studies found younger stellar populations in the smaller member of galaxy pairs (e.g., Krabbe et al. 2008, 2011; Alonso-Herrero et al. 2012). In order to check if this is also the case for our INT pairs, we calculated their mass ratios using the stellar masses obtained from the stellar population modelling and selected the ones where one of the galaxies is more than twice the mass of the other ($M_*^A > 2 M_*^B$). We found that 11 of the 18 pairs with spectra satisfy this criterion. Figure 13 shows the sum of light and mass fractions younger than 2 Gyr ($x_{[y,io]}$ and $m_{[y,io]}$) and the light- and mass-weighted mean stellar ages ($\langle t_* \rangle_L$ and $\langle t_* \rangle_M$) of the A and B members of the pairs. We find that the least massive galaxies in the pairs (B) have a median $x_{[y,io]} = 84 \pm 26\%$ and $\langle t_* \rangle_L = 8.7 \pm 0.5$, whilst the most massive (A) have $x_{[y,io]} = 54 \pm 35\%$ and $\langle t_* \rangle_L = 9.1 \pm 0.7$. In mass fractions, for the B galaxies in the pairs we measure a median $m_{[y,io]} = 53 \pm 40\%$ and $\langle t_* \rangle_M = 9.5 \pm 0.4$, and for the A galaxies a median $m_{[y,io]} = 11 \pm 32\%$ and $\langle t_* \rangle_M = 9.9 \pm 0.3$. Therefore, we find a higher fraction of young stellar populations (ages ≤ 2 Gyr) in the least massive galaxies of galaxy pairs with $M_*^A > 2 M_*^B$, although we cannot ensure that the distributions are different based on the KS-test p-values that we find (see Fig. 13).

Several publications also reported that both star formation and nuclear activity are enhanced with decreasing pair separation (e.g., Ellison et al. 2013; Satyapal et al. 2014; Steffen et al. 2023). Therefore we measured the projected separation between the two members of the 18 pairs using the r' band acquisition images (see Figs. 1 and A.1) and looked for possible trends in light- and mass-weighted stellar ages, SFRs, and/or the different BPT and WHAN diagrams considered in previous sections. Although in the case of our pairs we do not find any trend with projected distance between the pair members, we believe that this is due to the narrow range that they span, between 10 and 90 kpc, with 32 out of the 36 galaxies having projected separations ≤ 40 kpc (i.e., close pairs; Ellison et al. 2013).

8. Summary and conclusions

In this work we analysed spectroscopic observations of 95 galaxies from a parent sample of 100 galaxies in 43 interacting system candidates from the Arp & Madore (1987) catalogue. The selected galaxies are pairs and small groups. Most of them had no previous spectroscopic data.

We found that 60 galaxies are in real interacting systems, mainly in galaxy pairs and groups. A control sample of isolated galaxies was built using SDSS spectra of galaxies matched in redshift, absolute J magnitude, and galaxy morphology to the interacting sample. We compared the stellar populations and ionized gas properties of the two samples, INT and CTR, and found the following.

- More than half of the INT sample is dominated in light fractions by stellar populations younger than 2 Gyr. Interacting galaxies present a median fraction of these young stellar populations of 55%, compared to 28% found in the CTR sample. This difference is also found in mass fractions: 10% in the INT sample versus 3% in the CTR sample.
- We find higher stellar and nebular extinction in the interacting galaxies relative to the control sample. The median A_V^{gas} and A_V^* of the interacting sample are 2 and 2.6 times the ones found in the control sample. This suggests that our interacting galaxies are dustier.
- We find $A_V^{gas} > A_V^*$ in both the INT and CTR samples, although some INT galaxies have $A_V^{gas} \approx A_V^*$. These galaxies are the ones having the youngest stellar populations in the INT sample, which could explain their high A_V^* values.
- We found an excess of AGN in the INT sample relative to the CTR sample. Depending on the diagnostic diagrams employed and the number of INT and CTR sample galaxies considered, the fraction of AGN in the INT sample relative to the CTR sample ranges between 1.6 and 4.
- Considering the galaxy pairs in the INT sample having $M_*^A > 2 \times M_*^B$, we find that the least massive galaxies in the pairs

present higher fractions of stellar populations younger than 2 Gyr than the most massive galaxies.

Our study provides further observational evidence that interactions enhance star formation and nuclear activity in galaxies and therefore can have a significant impact on galaxy evolution.

Acknowledgements. PHC and CRA acknowledge support from project “Tracking active galactic nuclei feedback from parsec to kiloparsec scales”, with reference PID2022-141105NB-I00. PHC thanks to Conselho Nacional de Desenvolvimento Científico e Tecnológico (CNPq). RR acknowledges support from the Fundación Jesús Serra and the Instituto de Astrofísica de Canarias under the Visiting Researcher Programme 2023-2025 agreed between both institutions. RR, also acknowledges support from the ACIISI, Consejería de Economía, Conocimiento y Empleo del Gobierno de Canarias and the European Regional Development Fund (ERDF) under grant with reference ProID2021010079, and the support through the RAVET project by the grant PID2019-107427GB-C32 from the Spanish Ministry of Science, Innovation and Universities MCIU. This work has also been supported through the IAC project TRACES, which is partially supported through the state budget and the regional budget of the Consejería de Economía, Industria, Comercio y Conocimiento of the Canary Islands Autonomous Community. RR also thanks to Conselho Nacional de Desenvolvimento Científico e Tecnológico (CNPq), Proj. 311223/2020-6, 304927/2017-1, 400352/2016-8, and 404238/2021-1, Fundação de amparo à pesquisa do Rio Grande do Sul (FAPERGS, Proj. 16/2551-0000251-7 and 19/1750-2), Coordenação de Aperfeiçoamento de Pessoal de Nível Superior (CAPES, Proj. 0001). ACK thanks Fundação de Amparo à Pesquisa do Estado de São Paulo (FAPESP) for the support grant 2020/16416-5 and the Conselho Nacional de Desenvolvimento Científico e Tecnológico (CNPq). The authors thank Jose Andres Hernández Jimenez for helpful discussions. The authors thank the anonymous referee for useful and constructive suggestions.

References

- Abolfathi, B., Aguado, D. S., Aguilar, G., et al. 2018, *ApJS*, 235, 42
 Ahn, C. P., Alexandroff, R., Allende Prieto, C., et al. 2012, *ApJS*, 203, 21
 Alam, S., Albareti, F. D., Allende Prieto, C., et al. 2015, *ApJS*, 219, 12
 Alonso-Herrero, A., Rosales-Ortega, F. F., Sánchez, S. F., et al. 2012, *MNRAS*, 425, L46
 Araujo, B. L. C., Storchi-Bergmann, T., Rembold, S. B., Kaipper, A. L. P., & Dall’Agnol de Oliveira, B. 2023, *MNRAS*, 522, 5165
 Argudo-Fernández, M., Shen, S., Sabater, J., et al. 2016, *A&A*, 592, A30
 Argudo-Fernández, M., Yuan, F., Shen, S., et al. 2015, *Galaxies*, 3, 156
 Arp, H. C. & Madore, B. 1987, A catalogue of southern peculiar galaxies and associations (Cambridge University Press)
 Asari, N. V., Cid Fernandes, R., Stasińska, G., et al. 2007, *MNRAS*, 381, 263
 Azevedo, G. M., Chies-Santos, A. L., Riffel, R., et al. 2023, *MNRAS*, 523, 4680
 Baldwin, J. A., Phillips, M. M., & Terlevich, R. 1981, *PASP*, 93, 5
 Belfiore, F., Maiolino, R., Bundy, K., et al. 2018, *MNRAS*, 477, 3014
 Bessiere, P. S., Tadhunter, C. N., Ramos Almeida, C., & Villar Martín, M. 2012, *MNRAS*, 426, 276
 Bessiere, P. S., Tadhunter, C. N., Ramos Almeida, C., & Villar Martín, M. 2014, *MNRAS*, 438, 1839
 Bessiere, P. S., Tadhunter, C. N., Ramos Almeida, C., Villar Martín, M., & Cabrera-Lavers, A. 2017, *MNRAS*, 466, 3887
 Böhm, A., Wisotzki, L., Bell, E. F., et al. 2013, *A&A*, 549, A46
 Bruzual, G. & Charlot, S. 2003, *MNRAS*, 344, 1000
 Bundy, K., Bershadsky, M. A., Law, D. R., et al. 2015, *ApJ*, 798, 7
 Calzetti, D., Kinney, A. L., & Storchi-Bergmann, T. 1994, *ApJ*, 429, 582
 Cardelli, J. A., Clayton, G. C., & Mathis, J. S. 1989, *ApJ*, 345, 245
 Cid Fernandes, R. 2018, *MNRAS*, 480, 4480
 Cid Fernandes, R., González Delgado, R. M., García Benito, R., et al. 2014, *A&A*, 561, A130
 Cid Fernandes, R., Mateus, A., Sodré, L., Stasińska, G., & Gomes, J. M. 2005, *MNRAS*, 358, 363
 Cid Fernandes, R., Pérez, E., García Benito, R., et al. 2013, *A&A*, 557, A86
 Cid Fernandes, R., Stasińska, G., Mateus, A., & Vale Asari, N. 2011, *MNRAS*, 413, 1687
 Cid Fernandes, R., Stasińska, G., Schlickmann, M. S., et al. 2010, *MNRAS*, 403, 1036
 Cisternas, M., Jahnke, K., Inskip, K. J., et al. 2011, *ApJ*, 726, 57
 Copetti, M. V. F., Pastoriza, M. G., & Dottori, H. A. 1986, *A&A*, 156, 111
 Cortijo-Ferrero, C., González Delgado, R. M., Pérez, E., et al. 2017a, *A&A*, 607, A70
 Cortijo-Ferrero, C., González Delgado, R. M., Pérez, E., et al. 2017b, *A&A*, 606, A95
 Dametto, N. Z., Riffel, R., Pastoriza, M. G., et al. 2014, *MNRAS*, 443, 1754
 Davies, R. I., Burtscher, L., Rosario, D., et al. 2015, *ApJ*, 806, 127
 Donzelli, C. J. & Pastoriza, M. G. 1997, *ApJS*, 111, 181
 Eisenstein, D. J., Weinberg, D. H., Agol, E., et al. 2011, *AJ*, 142, 72
 Ellison, S. L., Mendel, J. T., Patton, D. R., & Scudder, J. M. 2013, *MNRAS*, 435, 3627
 Ellison, S. L., Patton, D. R., Mendel, J. T., & Scudder, J. M. 2011, *MNRAS*, 418, 2043
 Ellison, S. L., Viswanathan, A., Patton, D. R., et al. 2019, *MNRAS*, 487, 2491
 Fu, H., Steffen, J. L., Gross, A. C., et al. 2018, *ApJ*, 856, 93
 Gatti, M., Lamastra, A., Menci, N., Bongiorno, A., & Fiore, F. 2015, *A&A*, 576, A32
 González Delgado, R. M., Cerviño, M., Martins, L. P., Leitherer, C., & Hauschildt, P. H. 2005, *MNRAS*, 357, 945
 Heckman, T. M. & Best, P. N. 2014, *ARA&A*, 52, 589
 Hernández-Toledo, H. M., Cortes-Suárez, E., Vázquez-Mata, J. A., et al. 2023, *MNRAS*, 523, 4164
 Hwang, H. S., Elbaz, D., Dickinson, M., et al. 2011, *A&A*, 535, A60
 Jin, G., Dai, Y. S., Pan, H.-A., et al. 2021, *ApJ*, 923, 6
 Karouzos, M., Jarvis, M. J., & Bonfield, D. 2014, *MNRAS*, 439, 861
 Kauffmann, G., Heckman, T. M., Tremonti, C., et al. 2003, *MNRAS*, 346, 1055
 Kenney, J. F. 1939, Mathematics of statistics (D. van Nostrand)
 Kennicutt, Robert C., J. 1998, *ARA&A*, 36, 189
 Kennicutt, R. C. & Evans, N. J. 2012, *ARA&A*, 50, 531
 Kewley, L. J., Groves, B., Kauffmann, G., & Heckman, T. 2006, *MNRAS*, 372, 961
 Kewley, L. J., Heisler, C. A., Dopita, M. A., & Lumsden, S. 2001, *ApJS*, 132, 37
 Knapen, J. H., Cisternas, M., & Querejeta, M. 2015, *MNRAS*, 454, 1742
 Koss, M., Mushotzky, R., Veilleux, S., & Winter, L. 2010, *ApJ*, 716, L125
 Krabbe, A. C., Pastoriza, M. G., Winge, C., et al. 2011, *MNRAS*, 416, 38
 Krabbe, A. C., Pastoriza, M. G., Winge, C., Rodrigues, I., & Ferreiro, D. L. 2008, *MNRAS*, 389, 1593
 Krabbe, A. C., Rosa, D. A., Pastoriza, M. G., et al. 2017, *MNRAS*, 467, 27
 Leitherer, C., Schaerer, D., Goldader, J. D., et al. 1999, *ApJS*, 123, 3
 Lenz, D. D. & Ayres, T. R. 1992, *PASP*, 104, 1104
 Li, W., Nair, P., Irwin, J., et al. 2023, *ApJ*, 944, 168
 Lin, L., Patton, D. R., Koo, D. C., et al. 2008, *ApJ*, 681, 232
 Marian, V., Jahnke, K., Mechtley, M., et al. 2019, *ApJ*, 882, 141
 Martins, L. P., Rodríguez-Ardila, A., Diniz, S., Riffel, R., & de Souza, R. 2013, *MNRAS*, 435, 2861
 McAlpine, S., Harrison, C. M., Rosario, D. J., et al. 2020, *MNRAS*, 494, 5713
 Neistein, E. & Netzer, H. 2014, *MNRAS*, 437, 3373
 Osterbrock, D. E. & Ferland, G. J. 2006, Astrophysics of gaseous nebulae and active galactic nuclei (University Science Books)
 Pan, H.-A., Lin, L., Hsieh, B.-C., et al. 2019, *ApJ*, 881, 119
 Pastoriza, M. G., Donzelli, C. J., & Bonatto, C. 1999, *A&A*, 347, 55
 Patton, D. R., Carlberg, R. G., Marzke, R. O., et al. 2000, *ApJ*, 536, 153
 Pierce, J. C. S., Tadhunter, C., Ramos Almeida, C., et al. 2023, *MNRAS*, 522, 1736
 Pierce, J. C. S., Tadhunter, C. N., Gordon, Y., et al. 2022, *MNRAS*, 510, 1163
 Querejeta, M., Meidt, S. E., Schinnerer, E., et al. 2015, *ApJS*, 219, 5
 Raimundo, S. I., Malkan, M., & Vestergaard, M. 2023, *Nature Astronomy*, 7, 463
 Ramos Almeida, C., Bessiere, P. S., Tadhunter, C. N., et al. 2012, *MNRAS*, 419, 687
 Ramos Almeida, C., Tadhunter, C. N., Inskip, K. J., et al. 2011, *MNRAS*, 410, 1550
 Rembold, S. B., Riffel, R., Riffel, R. A., et al. 2024, *MNRAS*, 527, 6722
 Riffel, R., Mallmann, N. D., Ilha, G. S., et al. 2021, *MNRAS*, 501, 4064
 Riffel, R., Mallmann, N. D., Rembold, S. B., et al. 2023, *MNRAS*, 524, 5640
 Riffel, R., Pastoriza, M. G., Rodríguez-Ardila, A., & Bonatto, C. 2009, *MNRAS*, 400, 273
 Riffel, R., Pastoriza, M. G., Rodríguez-Ardila, A., & Maraston, C. 2008, *MNRAS*, 388, 803
 Robinson, T. G., Tadhunter, C. N., Axon, D. J., & Robinson, A. 2000, *MNRAS*, 317, 922
 Rosa, D. A., Milone, A. C., Krabbe, A. C., & Rodrigues, I. 2018, *Ap&SS*, 363, 131
 Ruschel-Dutra, D. & Dall’Agnol De Oliveira, B. 2020, danielrd6/ifscube: Modeling, Zenodo
 Ruschel-Dutra, D., Storchi-Bergmann, T., Schnorr-Müller, A., et al. 2021, *MNRAS*, 507, 74
 Sabater, J., Best, P. N., & Argudo-Fernández, M. 2013, *MNRAS*, 430, 638
 Sánchez, S. F. 2020, *ARA&A*, 58, 99
 Sánchez, S. F., Walcher, C. J., Lopez-Cobá, C., et al. 2021, *Rev. Mexicana Astron. Astrofis.*, 57, 3
 Sanders, D. B. & Mirabel, I. F. 1996, *ARA&A*, 34, 749
 Satyapal, S., Ellison, S. L., McAlpine, W., et al. 2014, *MNRAS*, 441, 1297
 Silva, A., Marchesini, D., Silverman, J. D., et al. 2021, *ApJ*, 909, 124
 Silverman, J. D., Kampczyk, P., Jahnke, K., et al. 2011, *ApJ*, 743, 2
 Skrutskie, M. F., Cutri, R. M., Stiening, R., et al. 2006, *AJ*, 131, 1163
 Spergel, D. N., Bean, R., Doré, O., et al. 2007, *ApJS*, 170, 377

- Stasińska, G., Cid Fernandes, R., Mateus, A., Sodré, L., & Asari, N. V. 2006,
MNRAS, 371, 972
- Steffen, J. L., Fu, H., Brownstein, J. R., et al. 2023, ApJ, 942, 107
- Steinborn, L. K., Hirschmann, M., Dolag, K., et al. 2018, MNRAS, 481, 341
- Storchi-Bergmann, T. & Schnorr-Müller, A. 2019, Nature Astronomy, 3, 48
- Strauss, M. A., Huchra, J. P., Davis, M., et al. 1992, ApJS, 83, 29
- Tacconi, L. J., Genzel, R., & Sternberg, A. 2020, ARA&A, 58, 157
- Tody, D. 1986, in Society of Photo-Optical Instrumentation Engineers (SPIE)
Conference Series, Vol. 627, Instrumentation in astronomy VI, ed. D. L.
Crawford, 733
- Tody, D. 1993, in Astronomical Society of the Pacific Conference Series, Vol. 52,
Astronomical Data Analysis Software and Systems II, ed. R. J. Hanisch,
R. J. V. Brissenden, & J. Barnes, 173
- Vazdekis, A., Koleva, M., Ricciardelli, E., Röck, B., & Falcón-Barroso, J. 2016,
MNRAS, 463, 3409
- Vazdekis, A., Sánchez-Blázquez, P., Falcón-Barroso, J., et al. 2010, MNRAS,
404, 1639
- Veilleux, S. & Osterbrock, D. E. 1987, ApJS, 63, 295
- Ventou, E., Contini, T., Bouché, N., et al. 2017, A&A, 608, A9
- Villforth, C. 2023, The Open Journal of Astrophysics, 6, 34
- Villforth, C., Hamann, F., Rosario, D. J., et al. 2014, MNRAS, 439, 3342
- Wesson, R. 2016, MNRAS, 456, 3774
- Woods, D. F. & Geller, M. J. 2007, AJ, 134, 527
- York, D. G., Adelman, J., Anderson, John E., J., et al. 2000, AJ, 120, 1579
- Yuan, F. T., Takeuchi, T. T., Matsuoka, Y., et al. 2012, A&A, 548, A117
- Yutani, N., Toba, Y., Baba, S., & Wada, K. 2022, ApJ, 936, 118
- Zaragoza-Cardiel, J., Smith, B. J., Rosado, M., et al. 2018, ApJS, 234, 35

Appendix A: INT and CTR samples additional material

The additional material in this appendix comprises the complementary images and spectra of the INT sample presented in Figs. A.1 and A.2. Furthermore, the following pages present tables of the INT and CTR samples. Table A.1 shows the information of the initial interacting candidates selected from the [Arp & Madore \(1987\)](#) catalogue. Table A.2 presents the confirmed INT galaxies radial velocities and their corresponding CTR galaxies selected from the SDSS. Tables A.3 and A.4 show the fluxes of the INT sample forbidden and permitted emission lines, respectively. Tables A.5 and A.6 present the same for the CTR sample. Finally, Tables A.7 and A.8 present the classifications with different diagnostic diagrams for the INT and CTR samples, respectively.

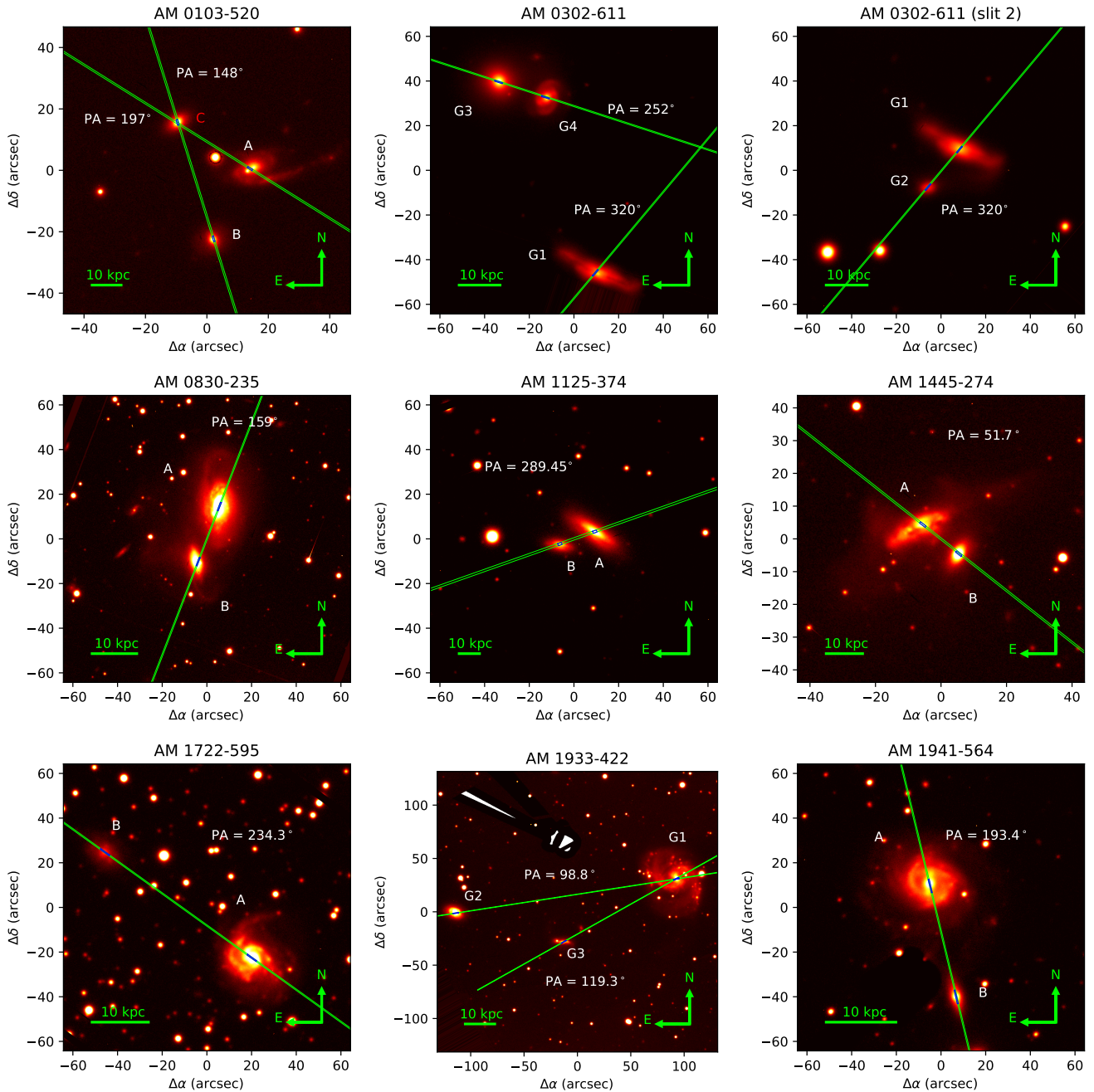
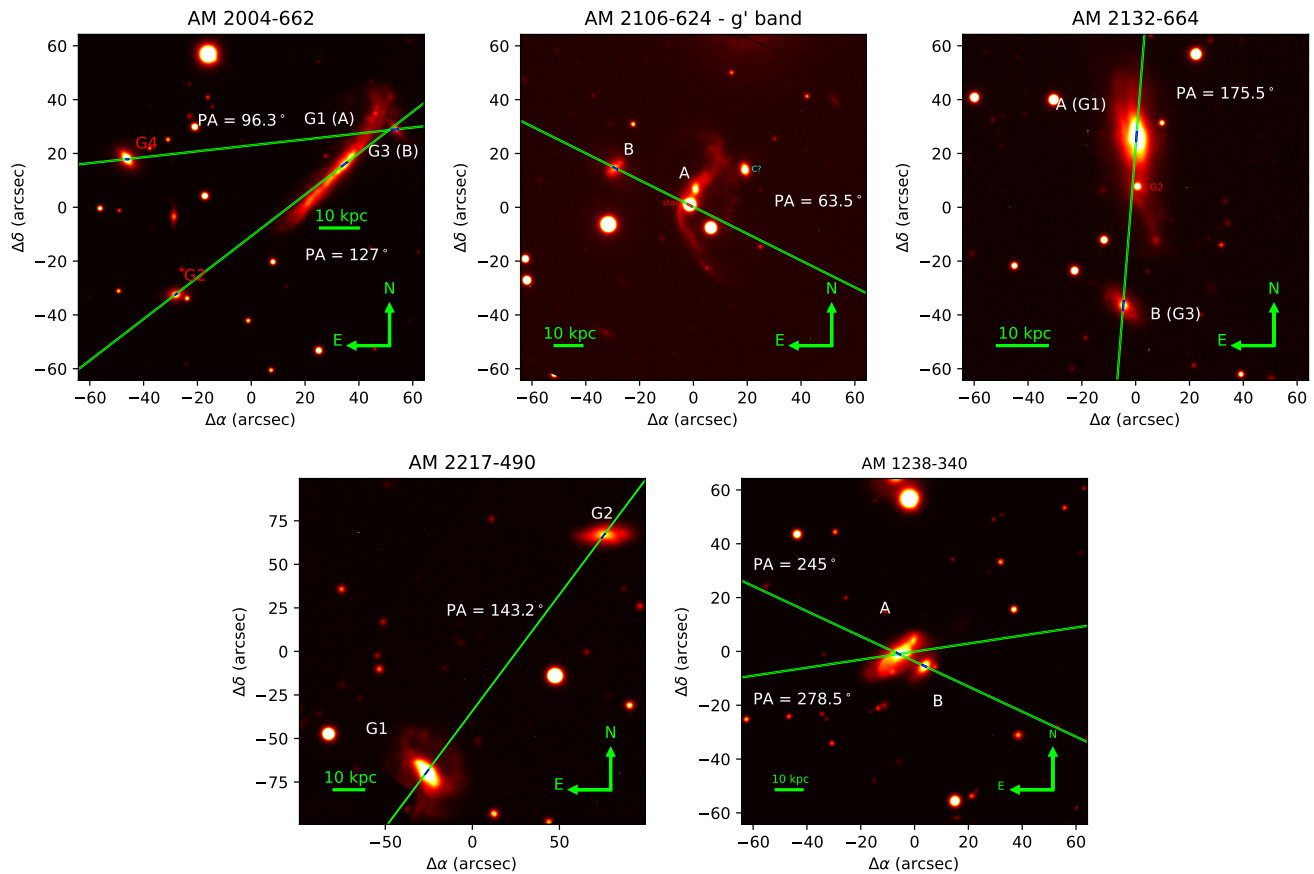
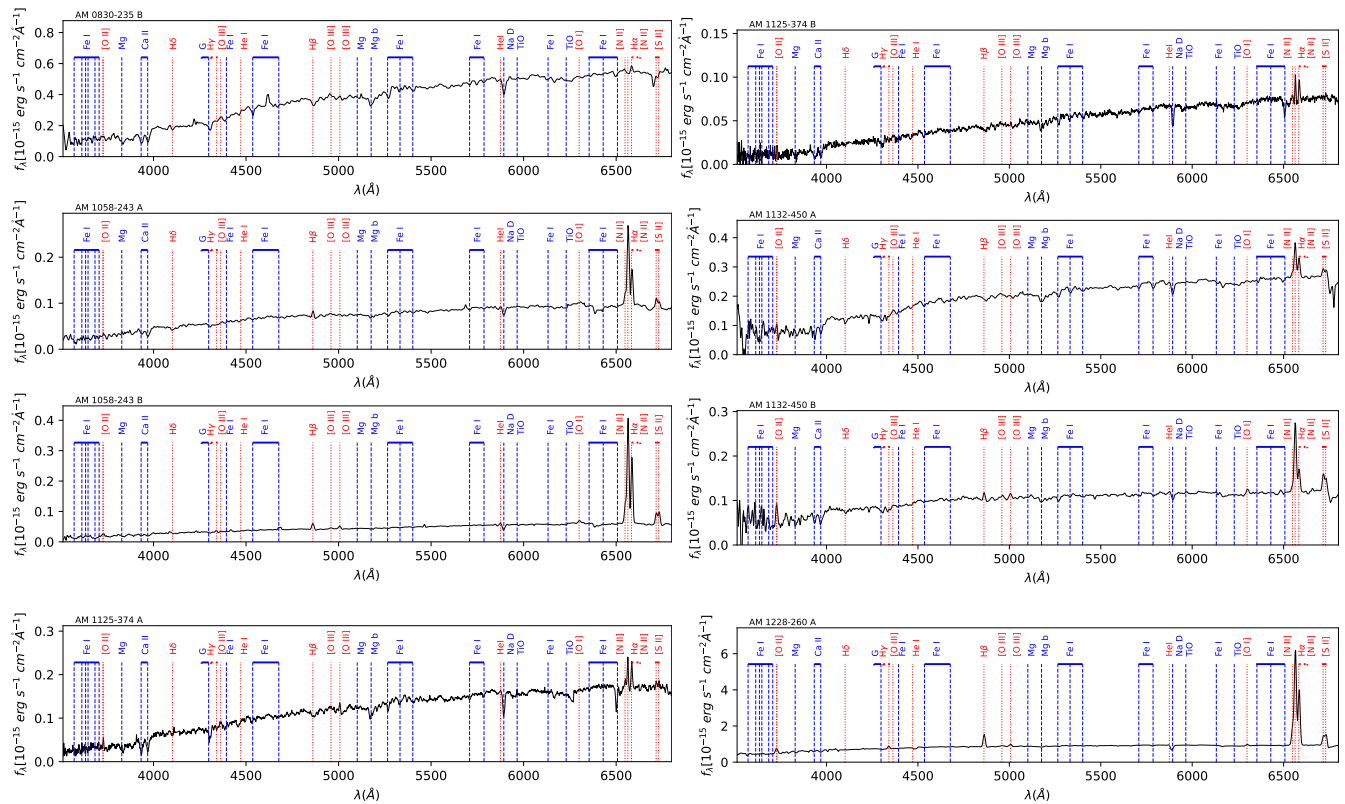


Fig. A.1. Same as in Fig. 1, but for the INT galaxies not included there.

**Fig. A.1.** continued.**Fig. A.2.** Same as in Fig. 2, but for the INT galaxies not included there.

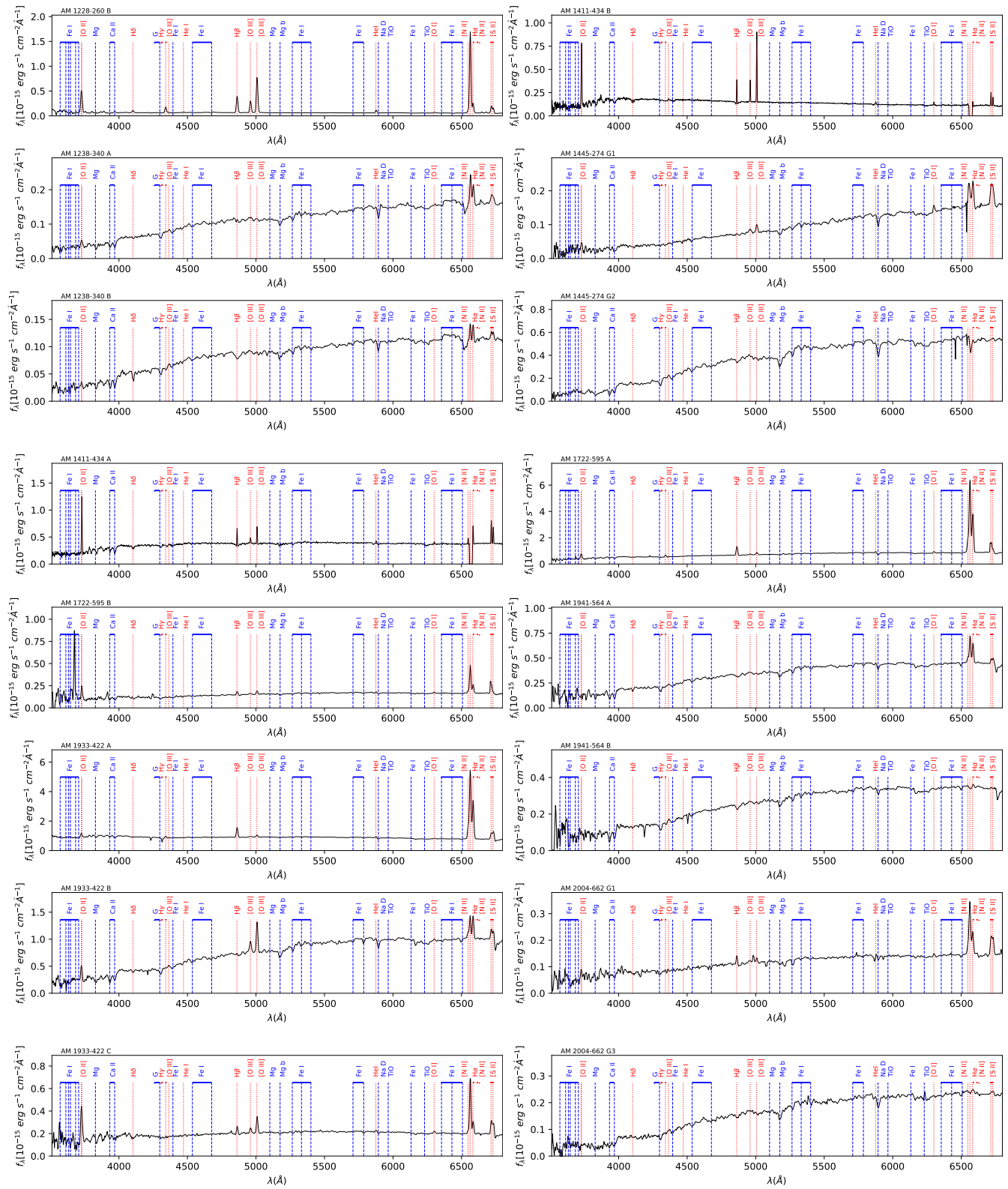
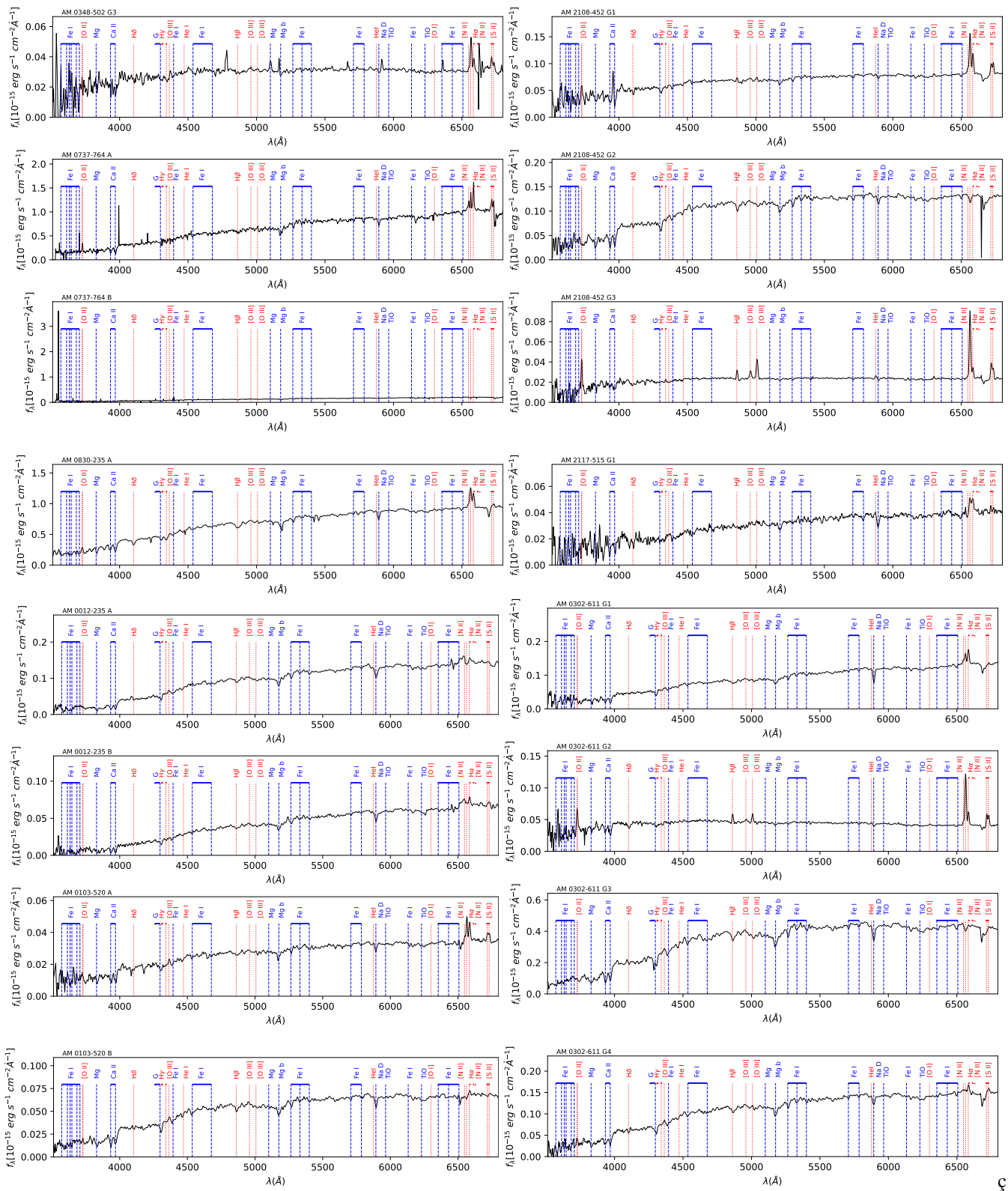


Fig. A.2. continued.

**Fig. A.2.** continued.

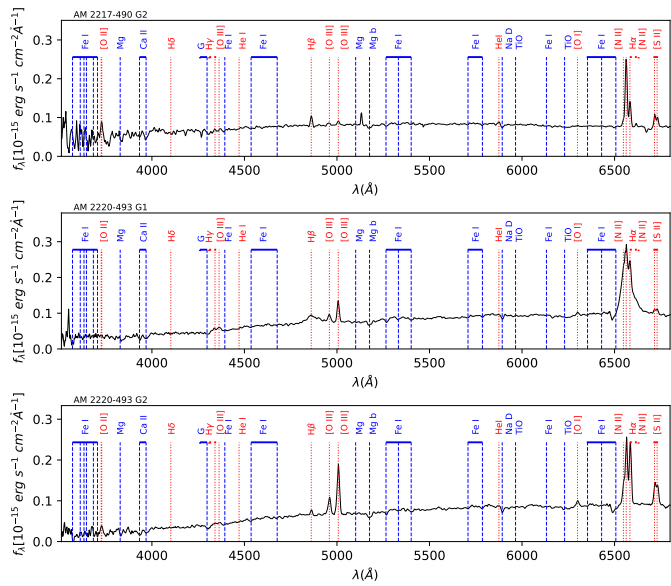


Fig. A.2. continued.

Table A.1. Interacting galaxies sample selected from the Arp & Madore Catalogue.

System Name (1)	Component (2)	α (2000) (hh:mm:ss)	δ (2000) (dd:mm:ss)	PA [°] (3)	Systemic velocity [km/s] (4)
AM 0012-235	A = LEDA 73318 B = 2MASX J00150913-2343541	00:15:10.230	-23:42:58.50	195.5	19076 >30000
AM 0103-520	A = ESO 195-30 B = LEDA 452921 C = Gaia DR3 4927464765788769536/ ESO 195-IG 030 NED02	01:05:51.320	-51:45:04.50	58/197	- - -
AM 0237-525	A = LEDA 128584 B = [MDS99] F154-017 LSBG F154-017	02:38:44.420	-52:46:39.10	220	- -
AM 0302-611	G1 = ESO 116-6 G2 = ESO 116-IG 006 NED02 G3 = 2MASX J03033046-6108201 G4 = 2MASX J03032756-6108281	03:03:30.430	-61:08:19.50	252/320	- - - 8553
AM 0305-824	A = LEDA 222825	03:01:44.9	-82:35:31	328	-
AM 0338-320	A = 6dFGS gJ034029.8-315142 B = 2MASX J03402854-3151520	03:40:29.660	-31:51:41.30	237	-
AM 0348-502	G1 = ESO 201-4 G2 = 2MASX J03502377-5018354 G3 = 2MASX J03501198-5017165	03:50:22.910	-50:18:09.00	343/305.5	10766 10940
AM 0737-764	A = ESO 35-11 B = WISEA J073520.20-765437.6	07:35:18.700	-76:54:52.09	200.5	5900
AM 0830-235	A = ESO 495-16 B = LEDA 86223	08:32:41.1	-24:02:32	159	7924
AM 0908-674	A = NGC 2788	09:09:03.394	-67:55:59.61	294	1641
AM 0952-273	A = LEDA 749047 B = LEDA 181883	09:54:56.750	-27:50:50.90	330	-
AM 1026-442	G1 - A = NGC 3261	10:29:01.263	-44:39:27.03	3	2563
AM 1058-243	A = LEDA 784699 B = WISEA J110049.40-245506.4	11:00:50.060	-24:55:07.89	276	22917
AM 1125-374	A = LEDA 615154 B = 2MASX J11273693-3757208	11:27:36.207	-37:57:18.13	289.45	17392
AM 1132-450	A = ESO 266-5 B = LEDA 35805	11:35:09.287	-45:23:15.97	165.7	5266
AM 1228-260	A = ESO 506-15 B = WISEA J123116.76-261741.1/ AM 1228-260 NED01	12:31:16.842	-26:17:29.93	2.9	5912
AM 1238-340	A = LEDA 88654 B = 2MASS J12404057-3421489	12:40:41.124	-34:21:47.75	245	16247
AM 1411-434	A = IC 4386 B = IC 4387	14:15:02.475	-43:57:39.94	184	1882
AM 1438-400	G1 = ESO 327-8 G2 = WISEA J144118.20-401956.4	14:41:20.089	-40:19:50.69	180 202	7825
AM 1445-274	G1 = ESO 448-2 G2 = WISEA J144852.47-275242.2	14:48:52.770	-27:52:38.17	51.7	14292
AM 1722-595	A = ESO 138-27 B = LEDA 367658	17:26:43.352	-59:55:55.17	234.3	6230
AM 1933-422	G1 = NGC 6806 G2 = 2MASX J19372362-4218194	19:37:05.0	-42:17:47	119.3 98.8	5733 5996
AM 1941-564	G3 = LEDA 3098348 A = IC 4890 B = WISEA J194534.04-563334.2	19:45:34.844	-56:33:04.92	193.4	5239
AM 2004-662	G1 = NAME McL A/ ESO 105-G026 G2 = WISEA J200937.54-661343.8 G3 = NAME McL B/	20:09:27.332	-66:12:55.63	127.6 96.3	11299 -

Notes. (1) System name according to Arp & Madore (1987) catalogue. (2) Galaxy identifier from Simbad (and NASA/IPAC Extragalactic Database - NED in case of divergency) when available. (3) Position angle of the observed slits. (4) NED systemic velocities for the galaxies with previous information.

Table A.1. continued.

System Name (1)	Component (2)	α (2000) (hh:mm:ss)	δ (2000) (dd:mm:ss)	PA [°] (3)	Systemic velocity [km/s] (4)
	WISEA J200924.36-661241.8				-
	G4 = LEDA 306574				-
AM 2024-525	G1 = ESO 186-51	20:28:16.548	-52:40:32.00	215.8	4912
	G3 = LEDA 64756				-
	G2 = 2MASX J20281941-5240587			283.5	16084
	G4 = LEDA 440336				-
	WISEA J202809.53-524037.6				-
AM 2031-500	A = ESO 234-49	20:35:20.907	-49:51:15.29	41	2579
	B = LEDA 65018				4561
AM 2036-510	G1 = FRL 908	20:40:03.800	-50:55:51.19	145.7	-
	G2 = ESO 234-62				4800
	G3 = 2MASS J20401226-5057017				-
AM 2037-550	A = ESO 187-1	20:41:27.90	-54:58:47.3	70	11446
AM 2038-323	G1 = NGC 6947	20:41:12.795	-32:30:13.22	24.8	5592
	G2 = LEDA 690531/				37171
	WISEA J204110.83-323106.8				-
AM 2057-650	A = ESO 107-2	21:01:17.64	-64:57:53.0	108.7	13720
	B = LEDA 317523				-
AM 2100-503	G1 = ESO 235-45	21:03:48.159	-50:21:52.19	289.4	4934
	G2 = 6dFGS gJ210341.7-502203			69	15233
	G3 = WISEA J210346.19-502146.2				-
AM 2106-624	G1 = ESO 107-9	21:10:06.84	-62:35:52.5	63.5	15761
	G2 = 2MASX J21101120-6235442				-
AM 2108-452	G1 = 2dFGRS TGS876Z088	21:11:34.35	-45:15:08.0	137,113.1,112.5	-
	G2 = ESO 286-73				9569
	G3 = LEDA 528634				-
	LCRS B210819.1-452815				-
AM 2117-371	G1 = 6dFGS gJ212026.9-370005	21:20:27.514	-37:00:04.88	274	
	APMUKS(BJ) B211720.70-371250.1				
	G2 = 6dFGS gJ212028.1-370005				31109
AM 2117-515	G1 - A = ESO 236-IG 005 NED01	21:21:14.09	-51:43:57.7	83	15471
	G2 - B = ESO 236-IG 005 NED02			5	-
	G3 - E = ESO 236-IG 005 NED03			285.5	-
	G4 - C = 2MASS J21211536-5143581			83	-
	G5 = 2MASS J21211361-5143535/			285.5	-
	(tadpole at NW of G3)				-
	G6 - D = LEDA 453396			5	-
	knots (See Fig. 1)			285.5	-
AM 2117-682	G1 = LEDA 127236	21:21:38.623	-68:10:05.06	273.8	25987
	G2 = 2MASS J21215262-6810066				-
	G3 = LEDA 287882				-
AM 2132-664	G1 - A = ESO 107-38	21:36:24.618	-66:28:50.10	175.5	8490
	G2 = 2MASS J21362448-6628496				-
	(Our images show that it is a star).				-
	G3 - B = LEDA 304337				-
AM 2137-515	A = ESO 236-31	21:41:17.04	-51:45:48.2	209	16765
	B = LEDA 453034				-
	WISEA J214120.56-514450.9				-
AM 2147-544	G1 = ESO 189-5	21:50:58.202	-54:33:08.56	229	8623
	G2 = LEDA 190556	21:51:00.125	-54:33:37.35		-
AM 2217-490	G1 = ESO 238-2	22:20:46.258	-48:45:17.43	143.2	9212
	G2 = 2MASX J22204151-4844140				9060
	G3 = LEDA 484571/				9081
	GALEXASC J222040.91-484242.0				-
AM 2220-493	G1 = ESO 238-6	22:23:13.043	-49:17:25.78	168	-
	G2 = LEDA 95417				17946
AM 2220-661	A = LEDA 127657	22:24:14.320	-66:02:15.70	75	10556

Notes. (1) System name according to [Arp & Madore \(1987\)](#) catalogue. (2) Galaxy identifier from Simbad (and NASA/IPAC Extragalactic Database - NED in case of divergency) when available. (3) Position angle of the observed slits. (4) NED systemic velocities for the galaxies with previous information.

Table A.1. continued.

System Name (1)	Component (2)	α (2000) (hh:mm:ss)	δ (2000) (dd:mm:ss)	PA [°] (3)	Systemic velocity [km/s] (4)
AM 2246-490	G1 = ESO 239-2 G2 = LEDA 482697/ PRC D-41	22:49:40.219	-48:51:01.92	322	12901

Notes. (1) System name according to [Arp & Madore \(1987\)](#) catalogue. (2) Galaxy identifier from Simbad (and NASA/IPAC Extragalactic Database - NED in case of divergency) when available. (3) Position angle of the observed slits. (4) NED systemic velocities for the galaxies with previous information.

Table A.2. Confirmed interacting pairs and groups. The second column presents the INT galaxies measured radial velocities. The third and fourth columns present the SDSS and astrophysical catalogues information of their control galaxies.

System name (1)	Radial velocity [km/s] (2)	SDSS DR9 Plate-Mjd-Fiberid (3)	CTR galaxy name (4)
AM 0012-235 A	18961 ± 92	2124-53770-0272	2MASX J14030448+2446252
B	18830 ± 95	2613-54481-0304	2MASX J12340843+1929256
AM 0103-520 ^{III} A	16345 ± 83	1693-53446-0629	2MASX J17053367+2506193
B	16441 ± 65	1601-53115-0280	LEDA 1389965
AM 0302-611 G1 (A)	8321 ± 97	2746-54232-0165	UGC 9185
G2 (D)	8509 ± 129	-	-
G3 (C)	8543 ± 54	1237663234989424850 ^{/*} (SDSS ObjId, no spectrum)	UGC 29
G4 (B)	8419 ± 83	2776-54554-0098	2MASX J14451344+1745338
AM 0338-320 A	29034 ± 102	0420-51871-0517	2MASX J00550203+1516012
B	29116 ± 179	0421-51821-0003	2MASX J01035856+1346065
AM 0348-502 G1 (A)	10707 ± 54	2774-54534-0448	IC 1021
G2 (B)	10759 ± 63	1607-53083-0452	LEDA 3090857
G3 (C)	10581 ± 116	1652-53555-0578	KISS F1530-273/WISEA J153423.63+295110.4
AM 0737-764 A	5899 ± 35	2352-53770-0006	NGC 3327
B	5875 ± 33	2515-54180-0046	LEDA 1557424
AM 0830-235 A	7838 ± 92	2234-53823-0120	NGC 4514
B	7628 ± 95	2130-53881-0553	2MASX J14230749+2835418
AM 1058-243 A	22782 ± 100	1937-53388-0453	LEDA 1853840
B	22881 ± 42	0731-52460-0345	LEDA 1396403
AM 1125-374 A	17075 ± 30	1771-53498-0483	2MASX J12593825+1510458
B	16851 ± 26	1588-52965-0534	LEDA 1847759
AM 1132-450 A	5226 ± 85	2132-53493-0224	IC 1006
B	5078 ± 63	2277-53705-0378	UGC 4504
AM 1228-260 A	5737 ± 83	1852-53534-0298	NVSS J160707+220337
B	5835 ± 76	-	-
AM 1238-340 A	15961 ± 94	1693-53446-0629	2MASX J17053367+2506193
B	16255 ± 82	-	-
AM 1411-434 A	1877 ± 45	1237680245198487603 ^{/*} (SDSS ObjId, no SDSS spectrum)	NGC 7497
B	1788 ± 38	2273-53709-27	UGC 4444
AM 1445-274 G1 (A)	14008 ± 83	2170-53875-0347	Z 107-41
G2 (B)	13847 ± 91	-	-
AM 1722-595 A	6119 ± 60	1929-53349-0372	IC 509
B	6162 ± 69	-	-
AM 1933-422 G1 (A)	5562 ± 128	0275-51910-0320	NGC 3339
G2 (B)	5582 ± 139	1776-53858-0098	LEDA 1429669
G3 (C)	5609 ± 84	2580-54092-0232	MCG+02-25-009
AM 1941-564 A	5130 ± 86	2350-53765-0539	NGC 3204
B	4787 ± 91	-	-
AM 2004-662 ^{III} A (G1)	11100 ± 220	2426-53795-0583	LEDA 1427577
B (G3)	10876 ± 101	-	-
AM 2036-510 G2 (A)	11792 ± 48	2523-54572-0428	LEDA 1390992
G1 (B)	12224 ± 92	1266-52709-0142	SDSS J081524.39+254729.7
G3 (C)	12018 ± 90	-	-
AM 2106-624 ^{III} G1 (A)	15761 ± 44	2759-54534-0160	IC 4410
G2 (B)	15382 ± 71	2227-53820-0018	LEDA 1785836
AM 2108-452 G2 (A)	9400 ± 77	2782-54592-0240	LEDA 1468533
G1 (B)	9633 ± 28	2126-53794-0075	2MASX J14164251+2854406
G3 (C)	9436 ± 50	0420-51871-0285	SDSS J004923.00+135600.9
AM 2117-515 G1 (A)	15053 ± 103	0860-53219-0120	LEDA 1866838
G2 (B)	15443 ± 178	2268-53682-0424	LEDA 1448216
G4 (C)	15293 ± 104	-	-
G5 (D)	15535 ± 56	-	-
G6 (E)	15396 ± 18	2765-54535-0129	2MASX J15065663+1426145
Central Knots	15305 ± 123	-	-
AM 2132-664 ^{IV} G1 (A)	8469 ± 130	2094-53851-0261	MCG+05-32-055
G3 (B)	8222 ± 43	-	-
AM 2217-490 ^V G1 (A)	9092 ± 57	2496-54178-0330	Z 126-20
G2 (B)	9003 ± 102	2599-54234-0571	IC 3615
AM 2220-493 G1 (A)	17832 ± 101	2764-54535-0355	MCG+03-38-035
G2 (B)	17746 ± 43	2518-54243-0066	2MASX J15503870+1530524

Notes. (1) System name and component according to [Arp & Madore \(1987\)](#) catalogue and Table A.1. (2) Systemic velocity obtained as described in Sec. 2.2. (3) Corresponding SDSS DR9 control partner. (4) Control galaxy identifier from Simbad (and NASA/IPAC Extragalactic Database - NED in case of divergency) when available. ^(II) AM 0103-520: C is not a member of the system. ^(III) AM 2004-662: G2 and G4 are foreground galaxies. ^(III) AM 2106-624: A = ESO107-009 is a member with radial velocity 15761 ± 44 km/s ([Strauss et al. 1992](#)), but we do not have the source spectra, because the slit was centred in a star. The A component CTR galaxy was not included in the next comparisons since we do not observe component G1. C (indicated in Fig. A.1) could be a member; however, it was not observed. ^(IV) AM 2132-664: Component G2 it is a star. ^(V) AM 2217-490: G3 (6dFJ2220410) is a member but was not observed. There is also a possible member towards the east of G1 (not in the image of Fig. A.1). ^(*) The control galaxy is not included in the INT versus CTR sample comparison as the spectrum of the control is unavailable in the SDSS DR9.

Table A.3 continued.

Object	[O II] λ 3726 flux $\times 10^{-15}$ [$erg\ s^{-1}\ cm^{-2}$]	[O III] λ 3729 flux $\times 10^{-15}$ [$erg\ s^{-1}\ cm^{-2}$]	[O III] λ 4363 flux $\times 10^{-15}$ [$erg\ s^{-1}\ cm^{-2}$]	[O III] λ 4959 flux $\times 10^{-15}$ [$erg\ s^{-1}\ cm^{-2}$]	[O III] λ 5007 flux $\times 10^{-15}$ [$erg\ s^{-1}\ cm^{-2}$]	[N II] λ 5755 flux $\times 10^{-15}$ [$erg\ s^{-1}\ cm^{-2}$]	He I λ 5876 flux $\times 10^{-15}$ [$erg\ s^{-1}\ cm^{-2}$]	[C I] λ 6300 flux $\times 10^{-15}$ [$erg\ s^{-1}\ cm^{-2}$]	[N II] λ 6548 flux $\times 10^{-15}$ [$erg\ s^{-1}\ cm^{-2}$]	[S II] λ 6583 flux $\times 10^{-15}$ [$erg\ s^{-1}\ cm^{-2}$]	[S II] λ 6716 flux $\times 10^{-15}$ [$erg\ s^{-1}\ cm^{-2}$]
AM2117-515 G5	22.57 \pm 0.32	19.95 \pm 0.28	0.13 \pm 0.04	18.42 \pm 0.17	54.62 \pm 0.44	-	1.22 \pm 0.05	0.48 \pm 0.02	0.99 \pm 0.03	2.58 \pm 0.1	3.09 \pm 0.04
AM2117-515 G6	7.93 \pm 1.48	15.53 \pm 1.36	-	-	2.02 \pm 0.08	0.17 \pm 0.02	0.89 \pm 0.02	0.28 \pm 0.02	1.06 \pm 0.07	6.49 \pm 0.13	3.64 \pm 0.12
AM2117-515 KNOTS	5.57 \pm 0.09	7.44 \pm 0.11	-	1.57 \pm 0.02	4.65 \pm 0.05	0.01 \pm 0.01	0.31 \pm 0.02	0.15 \pm 0.01	0.54 \pm 0.01	1.97 \pm 0.04	1.64 \pm 0.02
AM2132-664 G1	-	1118.5 \pm 195.36	-	45.26 \pm 4.25	214.86 \pm 19.94	23.48 \pm 2.19	18.27 \pm 0.69	24.11 \pm 2.1	160.98 \pm 3.84	489.88 \pm 3.33	57.75 \pm 6.4
AM2132-664 G3	10.85 \pm 0.34	8.17 \pm 0.37	-	1.08 \pm 0.03	3.78 \pm 0.04	0.31 \pm 0.01	0.34 \pm 0.06	0.28 \pm 0.02	1.17 \pm 0.11	2.85 \pm 0.06	1.83 \pm 0.03
AM2217-490 G1	119.29 \pm 1.38	86.34 \pm 2.0	-	17.55 \pm 0.19	54.88 \pm 0.45	1.37 \pm 0.07	2.57 \pm 0.12	4.52 \pm 0.21	31.39 \pm 0.51	96.85 \pm 0.5	25.56 \pm 0.55
AM2217-490 G2	4.31 \pm 0.08	7.69 \pm 0.1	-	0.32 \pm 0.03	1.29 \pm 0.06	0.12 \pm 0.02	0.4 \pm 0.02	0.03 \pm 0.01	0.99 \pm 0.07	3.7 \pm 0.05	1.75 \pm 0.03
AM2220-493 G1	323.44 \pm 111.18	307.94 \pm 107.54	199.97 \pm 8.83	313.74 \pm 4.51	815.01 \pm 18.33	1.36 \pm 0.18	-	15.85 \pm 0.57	93.82 \pm 1.66	86.71 \pm 1.61	25.3 \pm 0.59
AM2220-493 G2	15.04 \pm 3.34	26.59 \pm 3.07	-	30.26 \pm 0.65	88.12 \pm 1.12	0.49 \pm 0.1	0.91 \pm 0.13	3.24 \pm 0.11	13.06 \pm 0.13	35.43 \pm 0.25	12.84 \pm 0.31
											10.37 \pm 0.38

Notes. (1) System name and component according to [Arp & Madore \(1987\)](#) catalogue and Table A.1.

Table A.4. Extinction corrected permitted emission lines measurements in the INT sample.

Object (1)	Av [mag]	H δ flux x 10 $^{-15}$ [erg s $^{-1}$ cm $^{-2}$]	H γ flux x 10 $^{-15}$ [erg s $^{-1}$ cm $^{-2}$]	H β flux x 10 $^{-15}$ [erg s $^{-1}$ cm $^{-2}$]	H α flux x 10 $^{-15}$ [erg s $^{-1}$ cm $^{-2}$]	EW H α [Å]
AM0012-235 A	-	-	-	-	-	0.7±0.1
AM0012-235 B	-	-	-	-	-	1.0±0.1
AM0103-520 A	3.1±0.2	0.72±0.11	0.57±0.03	0.87±0.07	2.49±0.04	7.2±0.1
AM0103-520 B	-	-	-	-	-	0.3±0.1
AM0302-611 G1	5.6±0.1	121.45±5.04	59.88±3.04	14.6±0.61	41.9±0.44	4.9±0.0
AM0302-611 G2	1.8±0.1	0.23±0.05	0.69±0.04	1.51±0.06	4.32±0.03	27.9±0.2
AM0302-611 G3	-	-	-	-	-	0.0±0.0
AM0302-611 G4	4.9±0.4	-	-	3.54±0.44	10.17±0.79	1.8±0.1
AM0338-320 A	1.8±0.2	1.17±0.13	2.33±0.2	4.55±0.36	13.06±0.2	63.8±0.4
AM0338-320 B	2.7±0.2	0.5±0.06	0.65±0.05	0.8±0.04	2.29±0.05	11.0±0.2
AM0348-502 G1	1.0±0.2	0.19±0.03	0.77±0.04	1.48±0.07	4.24±0.03	9.2±0.0
AM0348-502 G2	2.2±0.1	3.68±0.12	6.62±0.25	15.24±0.59	43.75±0.25	81.4±0.4
AM0348-502 G3	3.4±0.2	2.32±0.59	0.33±0.1	1.49±0.09	4.29±0.04	11.0±0.1
AM0737-764 A	2.9±0.2	1.33±0.62	6.27±0.45	14.56±0.64	41.78±1.21	4.9±0.1
AM0737-764 B	-	-	-	-	-	0.0±0.0
AM0830-235 A	3.7±0.1	-	7.15±0.97	38.54±1.34	110.6±0.88	7.7±0.1
AM0830-235 B	4.5±0.2	-	-	5.72±0.16	16.42±1.02	1.0±0.1
AM1058-243 A	3.7±0.2	3.11±0.39	7.59±0.44	13.79±1.01	39.57±0.54	27.1±0.2
AM1058-243 B	5.5±0.3	52.9±8.28	83.73±9.39	95.81±9.51	274.98±6.05	75.4±0.4
AM1125-374 A	4.0±0.2	14.44±1.95	10.66±1.32	6.42±0.25	18.44±0.68	5.4±0.2
AM1125-374 B	3.2±0.2	1.75±0.29	1.65±0.26	1.13±0.09	3.25±0.06	4.0±0.1
AM1132-450 A	4.0±0.1	-	-	14.12±0.5	40.52±0.28	8.1±0.1
AM1132-450 B	3.0±0.1	3.1±0.45	1.77±0.54	8.38±0.19	24.05±0.09	21.9±0.1
AM1228-260 A	3.1±0.1	76.71±6.83	146.0±11.56	291.02±12.9	835.22±5.35	85.4±0.4
AM1228-260 B	2.2±0.1	7.58±0.6	17.55±0.9	38.67±1.74	110.98±0.86	382.3±2.3
AM1238-340 A	3.0±0.2	0.86±0.13	3.59±0.39	4.55±0.22	13.07±0.21	8.7±0.1
AM1238-340 B	4.8±0.1	-	11.5±0.54	6.79±0.32	19.49±0.22	4.9±0.1
AM1411-434 A	-	-	-	-	-	0.0±0.0
AM1411-434 B	-	-	-	-	-	0.0±0.0
AM1445-274 G1	4.2±0.4	16.45±1.83	-	13.36±1.67	38.33±1.62	10.6±0.3
AM1445-274 G2	-	-	-	-	-	0.0±0.0
AM1722-595 A	3.6±0.1	123.72±6.24	193.49±7.79	401.2±17.49	1151.44±6.92	90.9±0.4
AM1722-595 B	3.2±0.1	-	2.06±0.15	16.96±0.57	48.66±0.35	26.9±0.2
AM1933-422 A	2.9±0.1	57.96±3.41	74.36±3.03	201.02±7.77	576.94±3.2	85.5±0.4
AM1933-422 B	2.2±0.1	3.42±0.13	1.47±0.54	13.81±0.34	39.64±0.43	7.7±0.1
AM1933-422 C	2.3±0.1	6.13±0.49	6.18±0.35	13.55±0.52	38.9±0.24	35.3±0.2
AM1941-564 A	5.2±0.1	-	-	74.35±2.53	213.38±1.57	9.6±0.1
AM1941-564 B	1.8±0.3	-	-	0.51±0.05	1.46±0.1	1.1±0.1
AM2004-662 G1	1.8±0.1	1.76±0.15	1.92±0.06	4.34±0.2	12.45±0.07	22.8±0.1
AM2004-662 G3	1.7±0.4	0.11±0.03	-	0.31±0.03	0.88±0.07	1.1±0.1
AM2036-510 G1	1.4±0.2	-	-	1.49±0.02	4.27±0.27	5.0±0.3
AM2036-510 G2	2.1±0.2	3.66±0.16	5.83±0.28	14.51±0.72	41.64±0.35	66.3±0.4
AM2036-510 G3	2.7±0.1	4.87±0.45	8.19±0.42	20.38±0.85	58.48±0.42	94.3±0.6
AM2106-624 G2	7.4±0.2	-	-	233.27±13.23	669.48±6.17	19.6±0.1
AM2108-452 G1	2.4±0.1	0.83±0.2	2.22±0.13	2.53±0.09	7.27±0.04	14.9±0.1
AM2108-452 G2	-	-	-	-	-	0.0±0.0
AM2108-452 G3	2.2±0.1	0.67±0.03	1.16±0.08	1.65±0.07	4.74±0.04	40.7±0.3
AM2117-515 G1	1.8±0.1	-	0.22±0.04	0.31±0.01	0.88±0.01	6.0±0.1
AM2117-515 G2	2.4±0.2	-	1.53±0.19	4.86±0.28	13.96±0.13	43.3±0.2
AM2117-515 G4	3.5±0.1	6.24±0.67	4.64±0.37	6.07±0.23	17.41±0.1	35.0±0.2
AM2117-515 G5	2.0±0.1	1.92±0.13	4.67±0.27	11.02±0.49	31.62±0.4	280.2±3.2
AM2117-515 G6	3.4±0.2	1.72±0.08	1.2±0.04	6.77±0.42	19.43±0.21	39.7±0.3
AM2117-515 KNOTS	1.4±0.2	0.25±0.02	1.2±0.07	3.29±0.19	9.45±0.11	78.1±0.7
AM2132-664 G1	6.2±0.0	-	38.83±13.17	281.77±3.01	808.68±3.78	15.3±0.1
AM2132-664 G3	2.0±0.2	0.74±0.08	2.12±0.17	3.87±0.21	11.11±0.09	29.3±0.1
AM2217-490 G1	2.9±0.1	16.33±0.73	23.13±0.77	53.93±1.95	154.79±0.78	47.3±0.2
AM2217-490 G2	2.0±0.1	1.17±0.06	1.79±0.06	3.92±0.16	11.25±0.07	33.2±0.2
AM2220-493 G1	6.5±0.2	-	157.94±20.21	65.4±3.77	187.69±5.18	14.7±0.4
AM2220-493 G2	3.7±0.2	0.83±0.06	4.55±0.1	12.76±0.62	36.62±0.64	26.6±0.4

Notes. (1) System name and component according to [Arp & Madore \(1987\)](#) catalogue and Table A.1.

Table A.6. Extinction corrected permitted emission lines measurements in the CTR sample.

Object (1)	Av [mag]	H δ flux x 10 $^{-15}$ [erg s $^{-1}$ cm $^{-2}$]	H γ flux x 10 $^{-15}$ [erg s $^{-1}$ cm $^{-2}$]	H β flux x 10 $^{-15}$ [erg s $^{-1}$ cm $^{-2}$]	H α flux x 10 $^{-15}$ [erg s $^{-1}$ cm $^{-2}$]	EW H α [Å]
0275-51910-0320	1.3±0.1	2.58±0.11	3.86±0.24	6.2±0.09	17.79±0.16	38.8±0.3
0420-51871-0285	1.2±0.1	0.19±0.02	0.23±0.03	0.43±0.01	1.22±0.03	12.2±0.3
0420-51871-0517	1.3±0.1	1.02±0.05	1.8±0.05	4.09±0.1	11.73±0.14	25.7±0.3
0421-51821-0003	2.3±1.0	-	2.1±1.03	1.35±0.6	3.88±1.23	2.4±0.5
0731-52460-0345	1.5±0.2	1.48±0.32	1.29±0.25	2.06±0.14	5.92±0.09	4.5±0.1
0860-52319-0120	1.2±0.1	1.02±0.16	1.48±0.06	2.87±0.03	8.24±0.15	21.3±0.4
1266-52709-0142	2.2±1.1	-	4.59±2.42	1.11±0.62	3.18±1.07	1.5±0.2
1588-52965-0534	0.8±0.3	0.22±0.03	0.39±0.08	0.56±0.05	1.6±0.03	6.4±0.1
1601-53115-0280	1.0±1.2	0.75±0.52	0.77±0.47	0.45±0.28	1.3±0.5	2.1±0.3
1607-53083-0452	1.7±0.1	12.13±0.57	18.93±0.95	31.87±1.21	91.46±1.16	38.7±0.5
1652-53555-0578	0.1±0.1	0.07±0.04	0.11±0.01	0.37±0.0	1.05±0.01	19.3±0.2
1693-53446-0629	1.2±0.1	0.43±0.12	0.7±0.09	1.29±0.06	3.7±0.04	9.1±0.1
1771-53498-0483	2.1±0.3	7.06±1.43	7.32±1.15	15.23±1.42	43.71±3.27	15.9±1.1
1776-53858-0098	1.2±0.2	0.94±0.12	0.65±0.11	1.01±0.06	2.91±0.04	7.9±0.1
1852-53534-0298	2.5±0.1	24.06±2.7	28.45±1.76	37.19±0.78	106.75±1.28	21.1±0.3
1929-53349-0372	1.6±0.3	1.63±0.54	1.43±0.14	1.83±0.15	5.26±0.1	5.9±0.1
1937-53388-0453	3.2±0.3	11.58±1.86	13.86±1.81	12.56±1.1	36.04±0.83	5.9±0.1
2094-53851-0261	3.4±0.2	-	20.15±3.63	31.01±2.21	89.0±3.35	17.4±0.6
2124-53770-0272	-	-	-	-	-	0.4±0.1
2126-53794-0075	1.4±0.1	-	-	1.21±0.03	3.46±0.04	2.1±0.0
2130-53881-0553	2.0±0.2	16.02±0.76	23.83±0.79	36.83±2.26	105.7±2.22	19.9±0.4
2132-53493-0224	-	-	-	-	-	2.3±0.8
2170-53875-0347	1.2±0.3	0.55±0.14	0.23±0.13	0.96±0.09	2.76±0.08	2.9±0.1
2227-53820-0018	-	-	-	-	-	0.3±0.1
2234-53823-0120	1.6±0.3	3.05±0.53	2.22±0.21	2.79±0.28	8.01±0.2	4.5±0.1
2268-53682-0424	1.7±1.5	0.86±0.88	0.87±0.8	0.68±0.57	1.95±1.1	2.6±0.6
2273-53709-0027	1.0±0.1	2.12±0.3	1.69±0.02	2.21±0.03	6.36±0.11	11.0±0.2
2277-53705-0378	0.8±0.1	0.18±0.09	0.25±0.06	0.43±0.01	1.24±0.03	5.5±0.1
2350-53765-0539	1.5±0.1	8.18±1.22	8.68±0.56	12.66±0.4	36.35±0.5	12.5±0.2
2352-53770-0006	-	-	-	-	-	0.8±0.2
2426-53795-0583	1.9±0.1	2.69±0.35	4.66±0.08	7.44±0.23	21.36±0.19	21.0±0.2
2496-54178-0330	-	-	-	-	-	0.4±0.0
2515-54180-0046	0.0±0.1	0.56±0.06	0.93±0.01	1.77±0.02	5.09±0.07	48.9±0.7
2518-54243-0066	2.1±0.1	10.64±0.28	17.24±0.56	32.11±0.4	92.15±0.99	40.0±0.4
2523-54572-0428	2.1±0.1	5.97±0.39	9.63±0.4	17.57±0.37	50.42±0.45	30.8±0.3
2580-54092-0232	1.0±0.9	1.02±0.39	0.9±0.4	0.57±0.21	1.64±0.33	3.2±0.3
2599-54234-0571	0.9±0.2	0.31±0.04	0.47±0.04	0.8±0.04	2.29±0.03	5.6±0.1
2613-54481-0304	1.6±0.3	0.46±0.26	0.61±0.07	0.81±0.09	2.33±0.09	2.7±0.1
2746-54232-0165	3.4±0.3	10.48±3.74	7.61±1.2	4.16±0.38	11.95±0.22	2.0±0.0
2764-54535-0355	1.8±0.3	1.18±0.14	2.09±0.16	2.59±0.29	7.44±0.2	7.8±0.1
2765-54535-0129	2.6±0.1	8.41±1.55	10.2±1.5	13.67±0.49	39.23±0.24	16.7±0.1
2774-54534-0448	1.4±0.3	1.05±0.45	1.71±0.18	1.88±0.15	5.41±0.16	2.0±0.0
2776-54554-0098	3.5±1.6	12.29±13.48	5.47±6.5	4.82±4.79	13.83±8.44	2.3±0.2
2782-54592-0240	0.6±0.3	0.24±0.03	0.26±0.03	0.58±0.05	1.66±0.05	7.1±0.2
1693-53446-0629	1.2±0.1	0.43±0.12	0.7±0.09	1.29±0.06	3.7±0.04	9.1±0.1

Notes. (1) Control sample galaxies Plate-MJd-Fiberid information from SDSS DR9 and matched on Table A.2.

Table A.7. Classification of each galaxy from the INT sample using BPTs and WHAN diagrams, and the one obtained when we required the same classification in at least four out of the five diagrams.

Object (1)		[NII] BPT	[SII] BPT	[OI] BPT	[OII] BPT	WHAN	4/5 DGs
AM0012-235 A	-	-	-	-	-	RG	INC
AM0012-235 B	-	-	-	-	-	RG	INC
AM0103-520 A	Composite	SF	SF	SF	SF	sAGN	INC
AM0103-520 B	-	-	-	-	-	RG	INC
AM0302-611 G1	LINER	-	-	-	-	wAGN	INC
AM0302-611 G2	SF	SF	SF	SF	SF	SF	SF
AM0302-611 G3	-	-	-	-	-	RG	INC
AM0302-611 G4	Seyfert	LINER	-	-	-	RG	INC
AM0338-320 A	Composite	SF	SF	SF	SF	sAGN	INC
AM0338-320 B	Seyfert	Seyfert	SF	SF	SF	sAGN	INC
AM0348-502 G1	LINER	Seyfert	Seyfert	Seyfert	Seyfert	sAGN	AGN
AM0348-502 G2	Composite	SF	SF	SF	SF	sAGN	INC
AM0348-502 G3	SF	SF	-	-	-	SF	INC
AM0737-764 A	LINER	LINER	LINER	SF	wAGN	AGN	
AM0737-764 B	-	-	-	-	-	RG	INC
AM0830-235 A	Composite	SF	SF	SF	SF	sAGN	INC
AM0830-235 B	Seyfert	-	Seyfert	LINER	RG		INC
AM1058-243 A	SF	SF	LINER	LINER	sAGN		INC
AM1058-243 B	Composite	SF	SF	SF	SF	sAGN	INC
AM1125-374 A	Composite	SF	Seyfert	SF	wAGN	INC	
AM1125-374 B	Composite	SF	SF	SF	wAGN	INC	
AM1132-450 A	Composite	SF	SF	SF	SF	sAGN	INC
AM1132-450 B	SF	SF	SF	SF	SF	SF	SF
AM1228-260 A	SF	SF	SF	SF	SF	sAGN	SF
AM1228-260 B	SF	SF	SF	SF	SF	SF	SF
AM1238-340 A	Composite	SF	SF	SF	SF	sAGN	INC
AM1238-340 B	Composite	LINER	LINER	SF	wAGN	AGN	
AM1411-434 A	-	-	-	-	-	RG	INC
AM1411-434 B	-	-	-	-	-	RG	INC
AM1445-274 G1	Seyfert	LINER	LINER	LINER	sAGN	AGN	
AM1445-274 G2	-	-	-	-	-	RG	INC
AM1722-595 A	SF	SF	SF	SF	sAGN	SF	
AM1722-595 B	SF	SF	SF	SF	SF	SF	SF
AM1933-422 A	SF	SF	SF	SF	sAGN	SF	
AM1933-422 B	Seyfert	Seyfert	Seyfert	SF	sAGN	AGN	
AM1933-422 C	SF	SF	SF	SF	SF	SF	SF
AM1941-564 A	Composite	SF	-	-	sAGN		INC
AM1941-564 B	Seyfert	LINER	-	-	RG		INC
AM2004-662 G1	SF	SF	SF	SF	sAGN	SF	
AM2004-662 G3	LINER	LINER	-	-	RG		INC
AM2036-510 G1	Composite	LINER	Seyfert	LINER	wAGN	AGN	
AM2036-510 G2	SF	SF	SF	SF	SF	SF	SF
AM2036-510 G3	SF	SF	SF	SF	SF	SF	SF
AM2106-624 G2	Composite	SF	SF	SF	SF	sAGN	INC
AM2108-452 G1	SF	SF	SF	SF	sAGN	SF	
AM2108-452 G2	-	-	-	-	-	RG	INC
AM2108-452 G3	SF	SF	SF	SF	SF	SF	SF
AM2117-515 G1	LINER	SF	Seyfert	SF	wAGN	INC	
AM2117-515 G2	SF	SF	SF	SF	SF	SF	SF
AM2117-515 G4	SF	SF	SF	SF	SF	SF	SF
AM2117-515 G5	SF	Seyfert	SF	SF	SF	SF	SF
AM2117-515 G6	SF	SF	SF	SF	SF	SF	SF
AM2117-515 KNOTS	SF	SF	SF	SF	SF	SF	SF
AM2132-664 G1	Composite	SF	SF	SF	sAGN		INC
AM2132-664 G3	SF	SF	SF	SF	SF	SF	SF
AM2217-490 G1	Composite	SF	SF	SF	sAGN		INC
AM2217-490 G2	SF	SF	SF	SF	SF	SF	SF
AM2220-493 G1	Seyfert	Seyfert	Seyfert	Seyfert	sAGN	AGN	
AM2220-493 G2	Seyfert	Seyfert	Seyfert	Seyfert	sAGN	AGN	

Notes. (1) System name and component according to [Arp & Madore \(1987\)](#) catalogue and Table A.1.

Table A.8. Classification of each galaxy from the CTR sample using BPTs and WHAN diagrams, and the one obtained when we required the same classification in at least four out of the five diagrams.

Plate-MJd-Fiberid (1)	[NII] BPT	[SII] BPT	[OI] BPT	[OII] BPT	WHAN	4/5 DGs
0275-51910-0320	SF	SF	SF	-	SF	SF
0420-51871-0285	SF	LINER	-	-	SF	INC
0420-51871-0517	SF	SF	-	-	SF	INC
0421-51821-0003	Composite	SF	-	-	RG	INC
0731-52460-0345	Seyfert	LINER	Seyfert	SF	wAGN	AGN
0860-52319-0120	SF	SF	SF	SF	sAGN	SF
1266-52709-0142	Seyfert	LINER	-	-	RG	INC
1588-52965-0534	SF	SF	SF	SF	SF	SF
1601-53115-0280	Composite	-	LINER	SF	RG	INC
1607-53083-0452	Composite	SF	SF	SF	sAGN	INC
1652-53555-0578	SF	SF	Seyfert	SF	SF	SF
1693-53446-0629	SF	SF	-	-	sAGN	INC
1771-53498-0483	Composite	SF	SF	SF	sAGN	INC
1776-53858-0098	SF	SF	SF	SF	SF	SF
1852-53534-0298	SF	SF	SF	-	sAGN	INC
1929-53349-0372	-	-	-	-	SF	INC
1937-53388-0453	Composite	SF	SF	SF	wAGN	INC
2094-53851-0261	Composite	SF	SF	SF	sAGN	INC
2124-53770-0272	-	-	-	-	RG	INC
2126-53794-0075	Seyfert	LINER	-	-	RG	INC
2130-53881-0553	Seyfert	Seyfert	Seyfert	Seyfert	sAGN	AGN
2132-53493-0224	-	-	-	-	RG	INC
2170-53875-0347	Composite	SF	-	-	RG	INC
2227-53820-0018	-	-	-	-	RG	INC
2234-53823-0120	-	-	-	-	wAGN	INC
2268-53682-0424	LINER	SF	-	-	RG	INC
2273-53709-0027	-	-	-	-	SF	INC
2277-53705-0378	SF	SF	LINER	-	SF	INC
2350-53765-0539	SF	SF	SF	-	sAGN	INC
2352-53770-0006	-	-	-	-	RG	INC
2426-53795-0583	SF	SF	SF	SF	SF	SF
2496-54178-0330	-	-	-	-	RG	INC
2515-54180-0046	SF	SF	Seyfert	-	SF	INC
2518-54243-0066	Composite	SF	SF	SF	sAGN	INC
2523-54572-0428	SF	SF	-	-	sAGN	INC
2580-54092-0232	Composite	SF	LINER	-	wAGN	INC
2599-54234-0571	-	-	-	-	wAGN	INC
2613-54481-0304	LINER	Seyfert	Seyfert	LINER	RG	AGN
2746-54232-0165	LINER	LINER	SF	SF	RG	INC
2764-54535-0355	Composite	SF	-	-	sAGN	INC
2765-54535-0129	SF	SF	SF	SF	sAGN	SF
2774-54534-0448	LINER	LINER	SF	LINER	RG	RG
2776-54554-0098	Composite	-	-	-	RG	INC
2782-54592-0240	-	-	-	-	SF	INC
1693-53446-0629	SF	SF	-	-	sAGN	INC

Notes. (1) Control sample galaxies Plate-MJd-Fiberid information from SDSS DR9 and matched on Table A.2.

Appendix B: Excluded sources additional material

This appendix presents the information on the excluded sources from the initial interacting candidates sample of Table A.1. They were excluded for not being part of an interacting system or if there was insufficient information to confirm or discard their nature. The images and spectra of the galaxies are in Figs B.1 and B.2. Table B.1 presents their radial velocities and the reason why they were excluded. Finally, their forbidden and permitted emission line fluxes are shown in Tables B.2 and B.3, respectively.

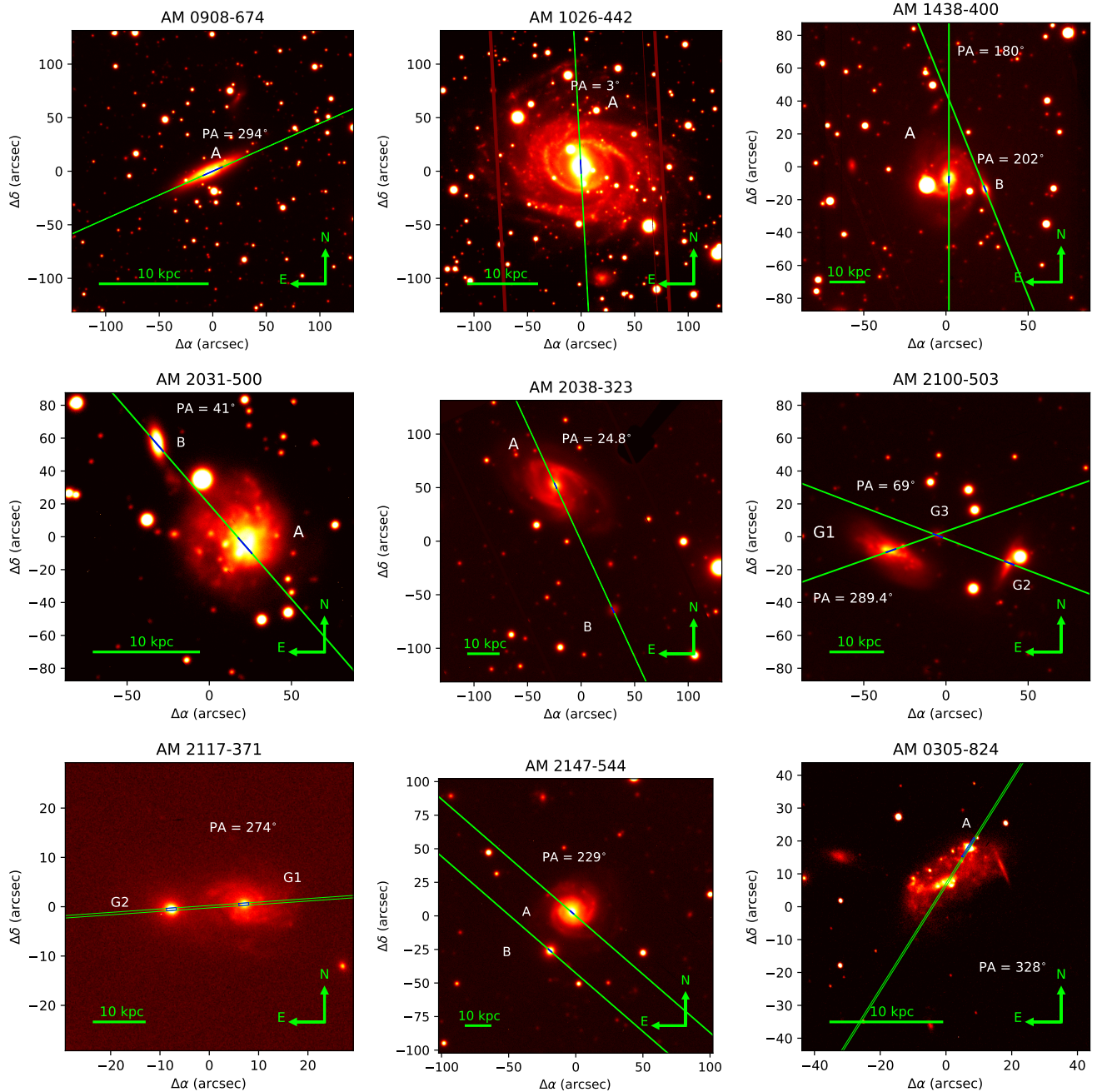


Fig. B.1. Same as in Fig. 1, but for the galaxies discarded as real pairs/groups.

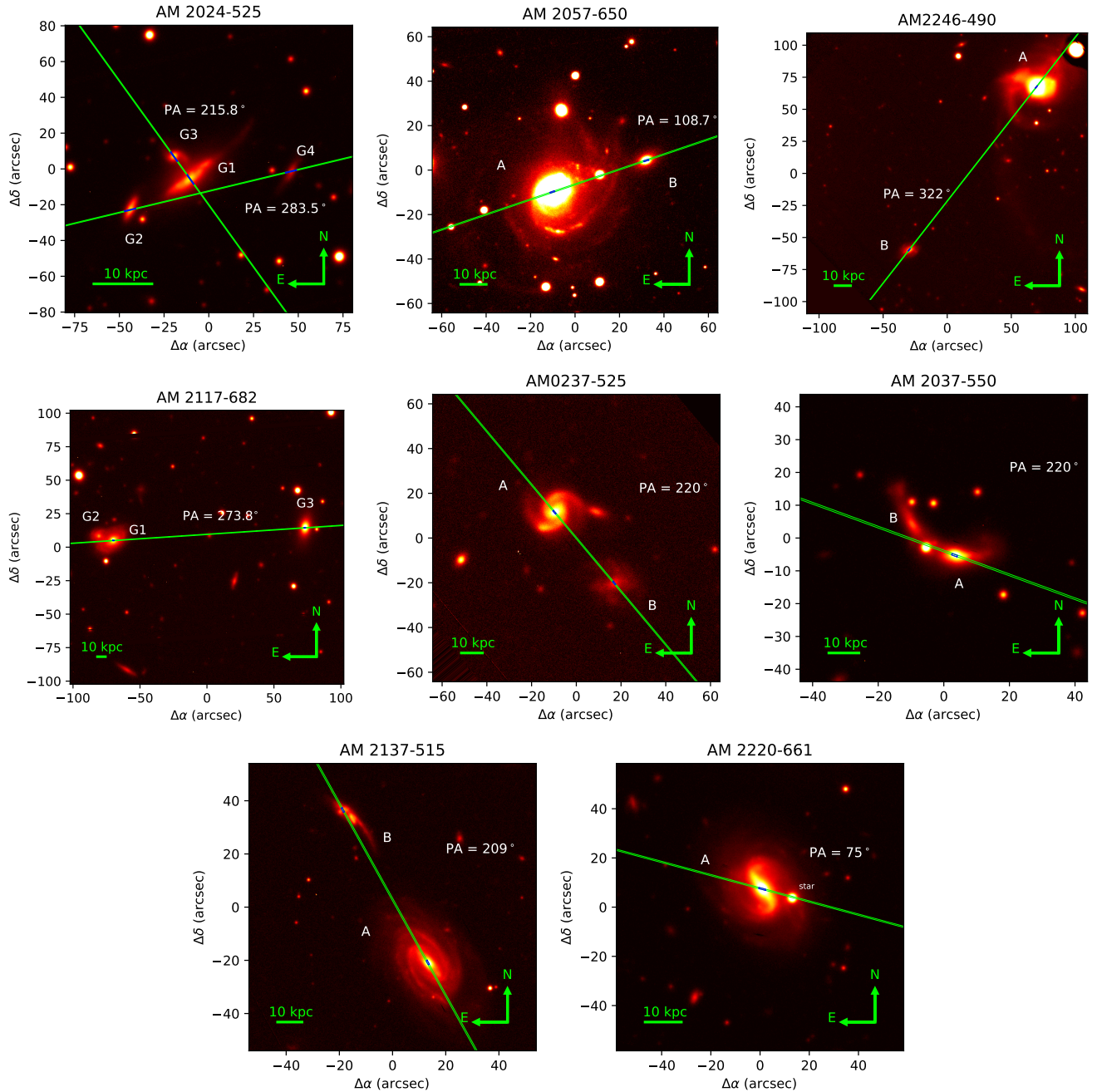


Fig. B.1. continue.

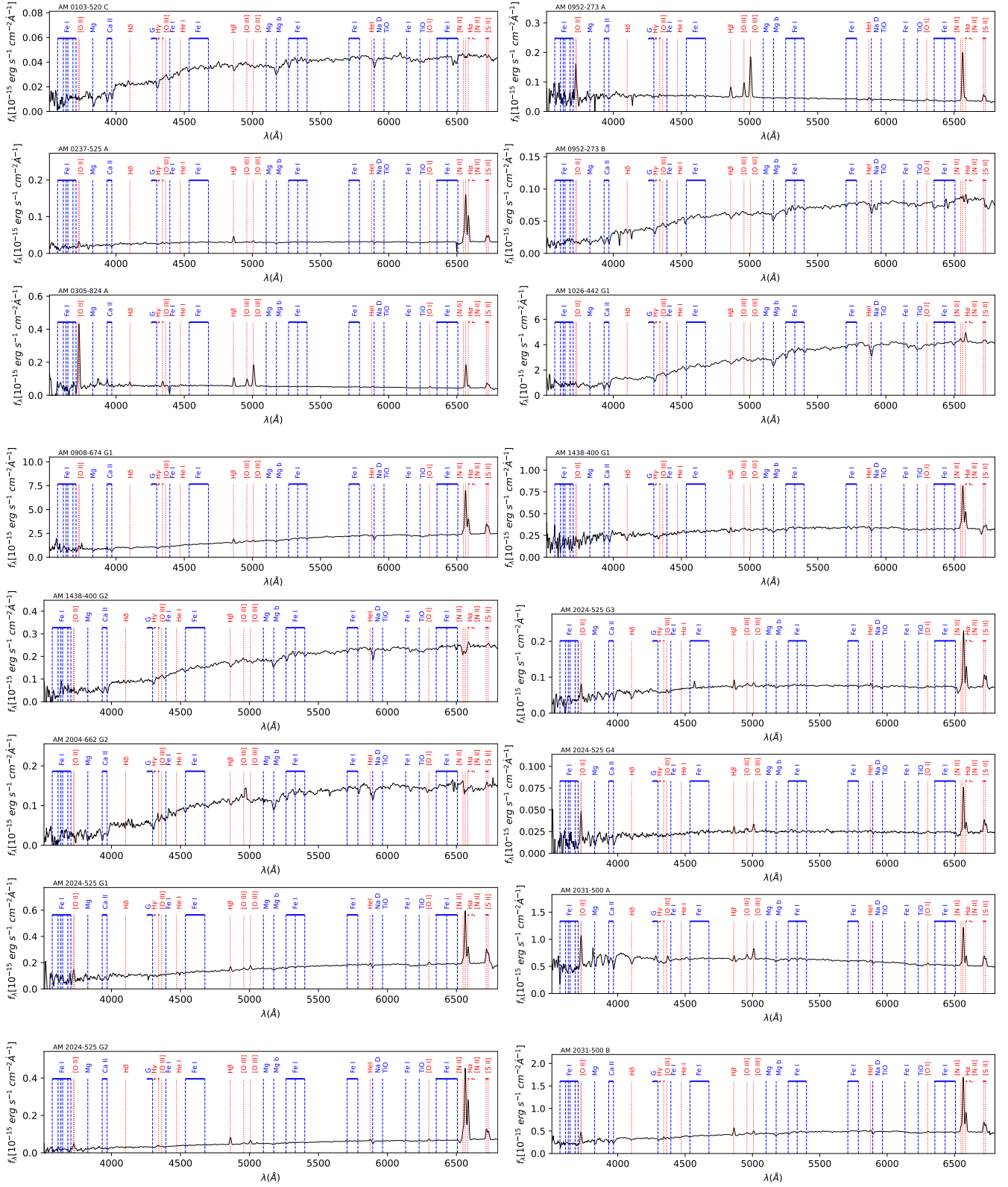


Fig. B.2. Same as in Fig. 2, but for the galaxies discarded as real pairs/groups.

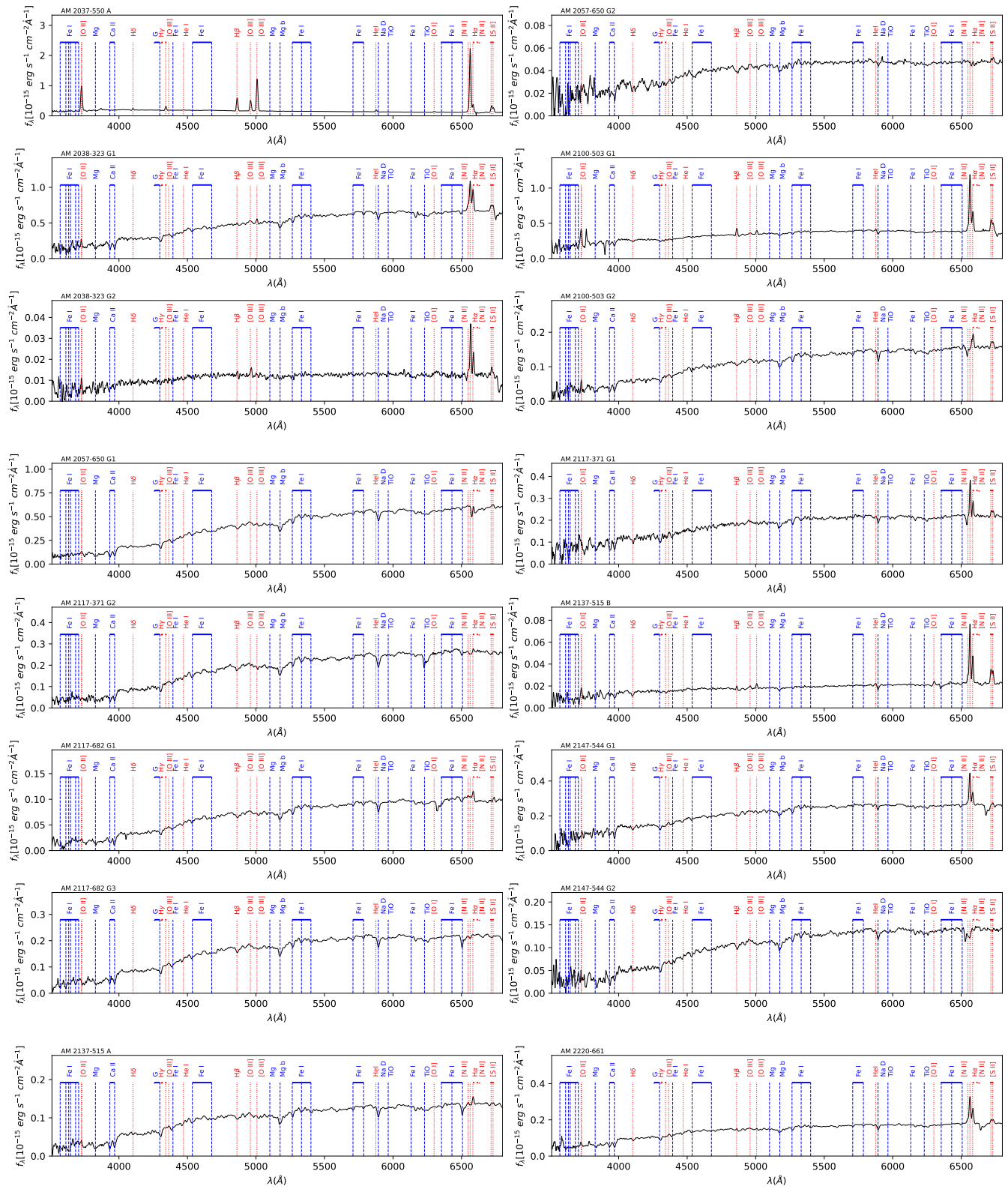
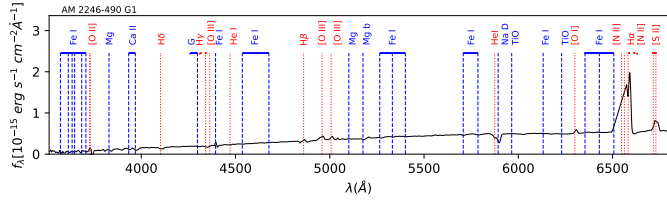


Fig. B.2. continued.

**Fig. B.2.** continued.**Table B.1.** List of non-physical, uncertain or not observed systems. The second column presents galaxies radial velocities when available.

System name (1)	Radial velocity [km/s] (2)	Comments
AM 0103-520 C	18576 ± 58	Not make part of the system.
AM 0237-525 A	16460 ± 57	Without a good S/N spectrum.
B		
AM 0305-824 A	4514 ± 105	Only this galaxy observed.
AM 0908-674 G1 (A)	1546 ± 126	Possible companion (not observed) towards NE.
B		It is a star towards the south-east of A.
AM 0952-273 A	4352 ± 86	It is not a pair.
B	19336 ± 88	
AM 1026-442 G1	2427 ± 75	Primary is NGC 3261. Two objects to the south were not observed.
AM 1438-400 G1	7684 ± 91	It is not a pair.
G2	14924 ± 86	
AM 2004-662 G2	27853 ± 84	It is a foreground galaxy.
G4	27977 ± 102	It is a foreground galaxy.
AM 2024-525 G1	4769 ± 82	Not make part of the system.
G2	15958 ± 106	Despite the redshifts, there are no signs of interaction and the galaxies are far apart.
G3	15924 ± 101	
G4	16061 ± 188	-
AM 2031-500 A	2433 ± 55	It is not a pair. A looks like a double or triple nucleus.
B	4488 ± 71	
AM 2037-550 A	11366 ± 68	We do not have a spectrum.
B		
AM 2038-323 G1 (A)	5566 ± 96	It is not a pair.
G2 (B)	36821 ± 123	
AM 2057-650 G1 (A)	13517 ± 94	B has faint continuum and no emission lines.
G2 (B)	13869 ± 97	Redshift is uncertain. The possible companion is at 36 arcsec north of A.
AM 2100-503 G1 (A)	4901 ± 107	It is not a group.
G2 (B)	15037 ± 87	
G3 (C)	$59459 \pm -$	
AM 2117-371 G1 (A)	15185 ± 83	It is not a pair.
G2 (B)	31066 ± 83	
AM 2117-515 G3		The slit does not go through the nucleus.
AM 2117-682 G1	25960 ± 81	It is not a group with G3.
G2	-	Close to G1. Not observed.
G3	16922 ± 94	
AM 2132-664 G2		Star towards the south of G1.
AM 2137-515 A	16899 ± 90	Not part of the pair.
B	24729 ± 95	B is likely a pair, no spectrum available.
AM 2147-544 G1 (A)	8614 ± 86	It is not a pair.
G2 - B	15747 ± 89	
AM 2220-661 A	10513 ± 109	It is not a pair. A spiral + star.
AM 2246-490 G1 (A)	$12684 \pm -$	Redshift is uncertain. The H α +NII is inside the CCD gap in both spectra.
G2 (B)	$12894 \pm -$	-

Notes. (1) System name and component according to [Arp & Madore \(1987\)](#) catalogue and Table A.1. (2) Systemic velocity obtained as described in Sec. 2.1

Table B.2. Extinction corrected emission lines measurements for forbidden and helium transitions of the excluded galaxies.

Object	[O II]λ3726 flux x 10 ⁻¹⁵ [erg s ⁻¹ cm ⁻²]	[O III]λ3729 flux x 10 ⁻¹⁵ [erg s ⁻¹ cm ⁻²]	[O III]λ4363 flux x 10 ⁻¹⁵ [erg s ⁻¹ cm ⁻²]	[O III]λ4959 flux x 10 ⁻¹⁵ [erg s ⁻¹ cm ⁻²]	[N II]λ5755 flux x 10 ⁻¹⁵ [erg s ⁻¹ cm ⁻²]	He I λ5876 flux x 10 ⁻¹⁵ [erg s ⁻¹ cm ⁻²]	[N II]λ6300 flux x 10 ⁻¹⁵ [erg s ⁻¹ cm ⁻²]	[N II]λ6548 flux x 10 ⁻¹⁵ [erg s ⁻¹ cm ⁻²]	[N II]λ6583 flux x 10 ⁻¹⁵ [erg s ⁻¹ cm ⁻²]	[S II]λ6716 flux x 10 ⁻¹⁵ [erg s ⁻¹ cm ⁻²]
	[erg s ⁻¹ cm ⁻²]	[erg s ⁻¹ cm ⁻²]	[erg s ⁻¹ cm ⁻²]	[erg s ⁻¹ cm ⁻²]	[erg s ⁻¹ cm ⁻²]	[erg s ⁻¹ cm ⁻²]	[erg s ⁻¹ cm ⁻²]	[erg s ⁻¹ cm ⁻²]	[erg s ⁻¹ cm ⁻²]	[erg s ⁻¹ cm ⁻²]
AM0103-520 C	32.96±19.95	13.60±8.41	-	2.85±1.27	-	-	-	1.84±0.6	2.57±0.83	1.7±0.51
AM0237-525 A	-	14.21±0.82	0.04±0.02	0.36±0.03	1.31±0.07	0.52±0.02	0.21±0.01	2.46±0.02	8.9±0.11	2.98±0.14
AM0305-824 A	2.52±0.04	2.73±0.05	-	0.61±0.01	1.88±0.02	0.05±0.01	0.08±0.01	0.21±0.01	0.48±0.03	1.83±0.18
AM0908-674 G1	770.12±184.0	973.48±179.4	-	26.57±2.2	149.64±9.19	5.3±1.49	38.5±4.92	172.56±9.56	637.24±4.38	0.28±0.02
AM0952-273 A	9.84±0.26	3.6±0.28	0.24±0.04	9.14±0.09	0.04±0.0	0.24±0.02	0.2±0.01	0.52±0.01	395.49±5.64	315.31±6.18
AM0952-273 B	367.42±85.53	417.4±89.53	51.04±25.12	2.37±0.84	41.07±3.25	6.03±0.88	11.25±1.21	7.51±0.82	35.15±1.77	0.54±0.05
AM1026-442 G1	83.18±11.03	25.86±9.24	-	6.28±0.82	23.07±2.03	5.12±0.8	-	-	61.56±3.11	48.52±2.68
AM1438-400 G1	17.9±1.45	5.8±1.16	-	0.76±0.12	0.83±0.12	1.6±0.11	-	6.79±0.34	20.85±0.18	5.0±0.19
AM1438-400 G2	-	-	-	-	-	-	-	-	-	-
AM2004-662 G2	-	-	-	-	-	-	-	-	-	-
AM2024-525 G1	208.77±7.22	116.19±9.8	-	5.96±0.14	22.43±0.98	1.2±0.14	4.48±0.3	4.28±0.22	10.55±0.48	31.64±0.39
AM2024-525 G2	90.25±1.98	84.8±2.21	6.45±0.19	21.71±0.22	0.82±0.2	4.33±0.2	2.46±0.14	18.0±0.31	17.14±0.2	12.97±0.21
AM2024-525 G3	5.56±0.21	6.73±0.26	-	0.69±0.04	1.48±0.06	-	0.34±0.05	0.18±0.0	3.45±0.07	1.86±0.03
AM2024-525 G4	6.0±0.16	6.21±0.16	-	0.48±0.07	1.44±0.04	0.05±0.01	0.14±0.02	0.12±0.01	0.14±0.03	0.73±0.02
AM2031-500 A	36.54±1.34	43.32±1.18	-	5.04±0.07	15.43±0.23	0.12±0.02	1.51±0.12	0.61±0.07	3.01±0.25	8.94±0.02
AM2031-500 B	76.2±1.96	59.68±1.62	-	2.89±0.13	13.75±0.64	1.98±0.12	3.37±0.26	0.72±0.22	13.38±0.71	9.06±0.19
AM2037-550 A	105.86±2.02	81.93±2.04	-	37.02±0.35	112.38±1.05	0.2±0.01	4.42±0.16	1.38±0.07	44.21±0.49	14.59±0.49
AM2038-323 G1	30.18±3.76	-	4.01±0.26	14.12±0.99	3.02±0.23	1.6±0.11	0.64±0.04	12.97±0.23	34.33±0.32	12.15±0.07
AM2038-323 G2	1.62±0.19	0.93±0.09	0.69±0.07	0.27±0.04	-	0.05±0.01	0.2±0.02	0.3±0.01	0.95±0.02	11.28±0.3
AM2057-650 G1	2.88±0.64	4.04±0.69	-	1.73±0.18	3.16±0.25	-	0.06±0.01	2.11±0.17	-	9.66±0.3
AM2057-650 G2	0.09±0.02	0.06±0.01	0.02±0.0	0.03±0.0	-	-	0.0±0.0	0.03±0.0	0.02±0.0	3.18±0.2
AM2100-503 G1	121.63±2.3	19.63±2.22	-	1.8±0.12	11.51±0.49	1.3±0.1	2.74±0.15	0.98±0.1	7.75±0.6	12.28±0.28
AM2100-503 G2	0.15±0.01	0.12±0.01	0.06±0.0	0.09±0.01	0.02±0.0	0.02±0.0	0.03±0.0	-	0.82±0.04	0.36±0.01
AM2117-371 G1	38.13±3.47	-	1.66±0.21	2.75±0.09	0.7±0.11	0.34±0.06	-	-	6.57±0.21	3.83±0.13
AM2117-371 G2	-	-	-	-	-	-	-	-	-	-
AM2117-682 G1	160.69±35.26	202.01±35.47	-	18.23±1.49	21.15±2.13	-	0.54±0.1	9.52±0.71	18.69±1.35	1.15±0.32
AM2117-682 G3	-	-	-	-	-	-	-	-	-	3.69±0.71
AM2137-515 A	3.66±0.44	1.34±0.4	-	0.4±0.05	0.65±0.06	-	0.1±0.01	0.25±0.02	0.69±0.08	0.73±0.06
AM2137-515 B	33.5±1.05	42.03±0.72	0.31±0.12	1.93±0.07	4.83±0.16	-	1.01±0.03	1.35±0.06	3.21±0.06	4.43±0.06
AM2147-544 G1	-	21.57±5.76	-	0.91±0.09	4.61±0.45	0.25±0.07	0.92±0.08	-	4.19±0.26	3.65±0.05
AM2147-544 G2	11.75±1.45	3.3±1.56	-	0.15±0.02	1.79±0.09	0.25±0.05	0.52±0.03	-	4.49±0.15	2.86±0.15
AM2220-661	-	-	-	37.27±2.15	32.39±2.08	4.26±0.49	-	7.26±1.75	312.25±12.41	3.05±0.15
AM2246-490 G1	34.18±6.93	57.21±6.9	-	-	-	-	-	-	424.09±21.63	80.68±2.46

Notes. (1) System name and component according to Arp & Madore (1987) catalogue and Table A.1.

Table B.3. Extinction corrected permitted emission lines measurements of the excluded galaxies.

Object (1)	Av [mag]	H δ flux x 10 $^{-15}$ [erg s $^{-1}$ cm $^{-2}$]	H γ flux x 10 $^{-15}$ [erg s $^{-1}$ cm $^{-2}$]	H β flux x 10 $^{-15}$ [erg s $^{-1}$ cm $^{-2}$]	H α flux x 10 $^{-15}$ [erg s $^{-1}$ cm $^{-2}$]	EW H α [Å]
AM0103-520 C	5.5±1.2	10.13±5.75	4.62±2.61	0.88±0.5	2.52±0.85	0.9±0.1
AM0237-525 A	3.0±0.1	2.73±0.31	3.55±0.27	6.09±0.27	17.47±0.12	58.1±0.3
AM0305-824 A	0.0±0.1	0.33±0.03	0.44±0.02	0.74±0.02	2.11±0.03	48.0±0.6
AM0908-674 G1	4.4±0.1	156.15±3.4	244.24±24.14	640.7±21.13	1838.8±10.71	28.1±0.1
AM0952-273 A	1.5±0.1	0.55±0.06	1.25±0.05	2.53±0.1	7.25±0.05	68.3±0.4
AM0952-273 B	7.4±0.4	-	203.76±26.33	20.38±2.92	58.5±4.27	2.9±0.2
AM1026-442 G1	2.8±0.4	44.01±3.7	-	12.67±1.76	36.35±2.47	1.1±0.1
AM1438-400 G1	2.7±0.1	4.59±1.03	9.54±1.01	19.83±0.78	56.92±0.34	24.0±0.1
AM1438-400 G2	-	-	-	-	-	0.0±0.0
AM2004-662 G2	-	-	-	-	-	0.0±0.0
AM2024-525 G1	4.0±0.1	22.09±0.64	21.02±0.47	43.13±1.39	123.79±0.89	31.1±0.2
AM2024-525 G2	4.2±0.1	15.07±0.39	20.0±1.47	42.59±2.03	122.24±0.9	76.1±0.4
AM2024-525 G3	2.0±0.2	-	1.4±0.18	3.58±0.29	10.26±0.16	31.3±0.2
AM2024-525 G4	2.3±0.2	0.23±0.05	0.53±0.07	1.38±0.1	3.95±0.05	30.9±0.2
AM2031-500 A	1.6±0.2	4.61±0.62	5.2±0.21	12.24±0.61	35.11±0.25	20.6±0.1
AM2031-500 B	2.6±0.1	12.21±0.79	21.99±0.67	43.19±1.84	123.94±0.99	36.2±0.2
AM2037-550 A	2.0±0.1	12.1±0.8	19.25±0.8	43.45±1.45	124.69±0.75	240.5±1.3
AM2038-323 G1	2.7±0.1	8.45±0.8	7.04±0.24	18.31±0.65	52.54±0.48	10.4±0.1
AM2038-323 G2	2.7±0.3	0.46±0.11	0.53±0.07	0.81±0.07	2.33±0.04	26.9±0.2
AM2057-650 G1	2.0±0.3	-	-	1.18±0.1	3.38±0.18	1.3±0.1
AM2057-650 G2	0.2±0.5	-	-	0.02±0.0	0.06±0.01	1.1±0.1
AM2100-503 G1	2.7±0.1	11.7±0.4	11.85±0.52	30.8±1.15	88.41±0.53	30.5±0.2
AM2100-503 G2	0.0±0.3	-	-	0.04±0.0	0.11±0.01	0.7±0.1
AM2117-371 G1	2.9±0.2	-	-	6.87±0.51	19.71±0.28	10.6±0.1
AM2117-371 G2	-	-	-	-	-	0.3±0.0
AM2117-682 G1	6.0±0.4	-	-	5.32±0.6	15.27±1.02	1.7±0.1
AM2117-682 G3	-	-	-	-	-	0.4±0.1
AM2137-515 A	2.6±0.4	0.37±0.06	0.58±0.07	0.34±0.04	0.98±0.07	1.1±0.1
AM2137-515 B	4.5±0.1	1.47±0.56	6.29±0.59	6.82±0.25	19.58±0.14	30.6±0.2
AM2147-544 G1	3.5±0.1	5.35±0.17	1.77±0.88	14.63±0.57	41.99±0.25	12.0±0.1
AM2147-544 G2	-	-	-	-	-	0.0±0.0
AM2220-661	2.9±0.1	1.96±0.35	4.06±0.12	7.2±0.32	20.67±0.23	13.2±0.1
AM2246-490 G1	3.4±0.2	-	7.7±1.07	48.26±3.33	138.5±4.44	20.0±0.6

Notes. (1) System name and component according to [Arp & Madore \(1987\)](#) catalogue and Table A.1.